Molecularly-guided spatial proteomics captures single-cell identity of the healthy and diseased nervous system

Sayan Dutta[1,2#], Marion Pang[1#], Gerard M. Coughlin[1,2], Sirisha Gudavalli[1], Michael L. Roukes[1,3,4], Tsui-Fen Chou[1], Viviana Gradinaru[1,2,5*]

[1]Division of Biology and Biological Engineering, California Institute of Technology, Pasadena, CA 91125
[2]Aligning Science Across Parkinson's (ASAP) Collaborative Research Network, Chevy Chase, MD 20815
[3]Division of Physics, Mathematics, and Astronomy, California Institute of Technology, Pasadena, CA 91125
[4]Division of Engineering and Applied Science, California Institute of Technology, Pasadena, CA 91125
[5]Howard Hughes Medical Institute, California Institute of Technology, Pasadena, CA 91125

[#]Contributed equally
*Corresponding author: Viviana Gradinaru (viviana@caltech.edu)

ORCIDs:
Sayan Dutta: 0000-0003-3577-2193
Marion Pang: 0000-0002-0158-2976
Gerard M. Coughlin: 0000-0003-0644-4721
Sirisha Gudavalli: 0009-0003-9091-8666
Michael L. Roukes: 0000-0002-2916-6026
Tsui-Fen Chou: 0000-0003-2410-2186
Viviana Gradinaru: 0000-0001-5868-348X

Abstract

Single-cell spatial proteomics (scSP) holds substantial potential for profiling healthy and diseased tissues. The emerging method of molecularly-guided unbiased scSP has mostly been applied to peripheral somatic tissues. Here, we optimize and apply scSP to the healthy and diseased mammalian brain, using molecularly-guided laser capture microdissection and unbiased mass spectrometry. We systematically evaluate the effects of tissue fixation, marker staining, and sample input size on proteome coverage and quantitative accuracy. We benchmark this workflow by profiling region-specific neuronal proteomes and describing the response of non-neuronal cells to acute brain injury. Across these applications, we integrate complementary transcriptomic resources to evaluate cross-modality trends and refine neuronal proteomic results by filtering out protein signals likely arising from non-neuronal cells, an essential consideration in heterogeneous tissues such as the brain. Finally, we leverage this approach to resolve proteomic differences between dopaminergic neuron subpopulations with differential vulnerability to Parkinson's disease and to uncover disease-specific disruptions in α-synuclein-aggregate-bearing single dopaminergic neurons. Together, these data demonstrate the utility of scSP in neuroscience research for understanding fundamental biology and the molecular drivers of neurological conditions.

50 **Introduction**

51 The central nervous system (CNS) is characterized by molecularly heterogeneous
52 neuronal cells that are spatially organized into distinct subpopulations defined by cell identity
53 and functional states [1]. Alongside neuronal subpopulations, the mosaic coexistence of glial cells
54 (i.e., astrocytes, microglia, and oligodendrocytes) also contributes to this intrinsic complexity.
55 Resolving such heterogeneity is critical for understanding both the healthy nervous system as
56 well as diseases with sparse pathology[2,3], requiring approaches that preserve spatial
57 information while enabling molecular profiling at the single-cell resolution. Moreover, human
58 nervous system samples from diseased subjects and small brain regions are often fixed for
59 archiving and available only in limited quantities, making fixation- and single-cell-compatible
60 approaches especially valuable.

61 Numerous single-cell analysis techniques have been employed to study brain cell types
62 and neurological diseases in a spatially resolved context, although most have focused on
63 transcriptomic insights[4-6]. Protein-focused spatial methods have allowed multiplexed detection
64 of predefined protein targets while preserving spatial context, providing valuable insights into
65 nervous system biology at the single-neuron level[7-9]. Such approaches are particularly powerful
66 for hypothesis-driven analyses, enabling targeted interrogation of known markers across
67 complex tissues and offering functional insights not always evident at the transcript level.
68 Complementary spatial mass spectrometry (MS)-based methods enable unbiased, discovery-
69 scale proteomic profiling directly from brain tissue and have yielded promising insights in
70 neuroscience[2,10-12]; however, these studies have thus far relied on region-level sampling and
71 have not been applied at single-cell resolution. In parallel, recent advances in MS sensitivity and
72 low-input sample preparation have now made it possible to approach single-cell proteomic
73 measures[13-18]. Recent studies have demonstrated that imaging-guided sample selection,
74 combined with laser-capture microdissection (LCM) or laser ablation and ultrasensitive MS, can
75 recover discovery-scale proteomes with spatial context from individual cells in archival fixed
76 peripheral tissue such as liver and pancreas[19,20]. Despite recent technical advances,
77 molecularly-guided, unbiased single-cell spatial proteomics has not yet been applied to the
78 mammalian nervous system.

79 Here, we address this gap by presenting a molecularly-guided LCM-based single-cell
80 spatial proteomics (scSP) workflow optimized for paraformaldehyde-fixed brain tissue. We show
81 that unbiased scSP can be applied to interrogate molecular heterogeneity within the mammalian
82 CNS. We explore the potential and constraints of this approach by studying region-specific
83 neuronal identities and describing neuroimmune alterations following focal brain injury. These

84 findings are contextualized within established biological frameworks and through integrative
85 multi-omics analyses, in which single-cell transcriptomic data inform refinement of cellular-origin
86 of proteomic assignments and enable cross-omics comparisons such as regional expression
87 trends between cortex and substantia nigra pars compacta (SNpc). Finally, we apply this
88 platform to define proteomic signatures associated with dopaminergic subtype vulnerability and
89 α-synuclein (αSyn) pathology in a mouse model of Parkinson's disease (PD), highlighting the
90 broader translational potential of LCM-based scSP for studying disease mechanisms *in vivo*.

91 **Results**

92 **Molecularly-guided single-cell spatial proteomics (scSP) enables robust proteomic**
93 **profiling across fixation conditions, staining parameters, and input sample sizes**

94 For unbiased mapping of the proteome from single cells of fixed brain tissue, we
95 adapted[20,21] a workflow that integrates molecularly-guided selection of micro-tissue samples for
96 downstream proteomic analysis **(Fig. 1A)**. Our workflow begins with tissue fixation, and cryo-
97 sectioning at 30 µm, followed by immunofluorescent (IF) or RNA-fluorescence in-situ
98 hybridization (FISH) staining to label cells of interest, facilitating marker or pathology-guided
99 selection for proteomic analysis. Targeted cells are then precisely isolated using LCM and
100 processed using a sample preparation workflow optimized for low-input, single-cell proteomic
101 analysis[21,22].

102 Before employing stain-guided isolation and processing of samples from fixed tissue, we
103 first assessed whether tissue fixation impacts downstream proteome coverage or introduces
104 bias in detected peptides. Bulk comparison of mouse brain fresh-frozen and fixed tissue,
105 acquired using data-dependent acquisition (DDA), revealed largely overlapping proteome
106 coverage, with 2,024 shared proteins, 175 unique to fixed tissue, and 155 unique to frozen
107 tissue **(Fig. 1B)**. Although statistical testing identified significant differences and the overall log
108 protein abundance correlation was moderate (R^2 = 0.70; **Fig. 1B, bottom**), no evidence of
109 systematic extraction bias from any cellular compartment was observed between conditions
110 **(Supp. Fig. 1A)**.

111 We next extended this approach to determine whether IF or RNA-FISH staining
112 protocols introduce measurable proteomic bias. Cortical tissue was stained using anti-NeuN
113 antibody as a representative protein marker **(Fig. 1C)** and FISH probes targeting glutamate
114 decarboxylase 1 and 2 (GAD1+GAD2) mRNA as a representative RNA marker **(Fig. 1D)**.
115 Comparative analysis was first performed at the bulk proteomic level (using DDA) and
116 subsequently at the single-neuron level using data-independent acquisition (DIA). For both IF-
117 and RNA-FISH-stained samples, bulk proteomes **(Supp. Fig. 1B, 1D)** and single-cell proteomes
118 **(Fig. 1, C, D, Supp. Fig. 1C, 1E)** showed substantial overlap with their respective unstained
119 controls, with comparable protein identifications per cell. Proteins detected uniquely in bulk
120 tissue by IF and RNA-FISH were predominantly low-abundance species, consistent with
121 stochastic sampling effects inherent to DDA rather than systematic staining-related bias **(Supp.**
122 **Fig. 1B, 1D)**. Log protein abundance values for single-cell analysis were strongly correlated
123 between stained and control samples (R^2 = 0.97 for IF; R^2 = 0.96 for HCR), indicating minimal
124 staining-induced bias **(Fig. 1C, 1D)**. Together, these results demonstrate that our IF and RNA-

125 FISH protocols do not introduce systematic bias in proteome coverage or protein abundance
126 and therefore can be confidently employed to define cellular populations within tissues of
127 interest from fixed tissue without compromising the integrity of downstream proteomic
128 measurements.

129 Next, we evaluated the impact of sample size on proteome coverage and quantification,
130 given that spatial proteomic investigation of the CNS might require samples larger than a single
131 cell in an ROI, or a combination of multiple ROIs. To probe the effect of varying ultra-low input
132 material size, tissue samples corresponding to increasing neuronal cell-body counts were
133 isolated from NeuN stained mice cortex by LCM (due to the finite resolution of cold laser
134 ablation, the effective excised areas were smaller than the nominal cut regions): single cells
135 (~800 μm^2), ~3 cells (2,000 μm^2), ~6 cells (5,000 μm^2), ~12 cells (10,000 μm^2), and ~25 cells
136 (20,000 μm^2) **(Fig. 1E, Supp. Fig. 2A-C)**. All samples were analyzed using a previously
137 optimized 1-hour LC-MS gradient with DIA[22,23], which was specifically tuned for single-cell
138 inputs. Notably, single-cell samples (n = 20 single cells) yielded consistently high proteome
139 depth, with up to ~2,200 proteins quantified from an individual neuron and protein identifications
140 increased with sampled area but plateaued beyond 10,000 μm^2 **(Fig. 1F)**. A similar pattern was
141 observed for the peptide quantification **(Supp. Fig. 2D)**. Higher coefficients of variation (CVs) in
142 single-cell samples relative to larger sampled areas from the cortex **(Fig. 1G)** likely reflects
143 biological heterogeneity unmasked at single-cell resolution.

144 Because single-cell measurements operate in a lower signal-to-noise regime than multi-
145 cell samples, we next assessed whether protein abundance scales proportionally with sampled
146 area. Protein abundance was modeled using a log-log scaling relationship, where the slope β_1
147 represents the scaling exponent. After removal of contaminants **(Supp. Fig. 2E)**, the mean
148 value of β_1 across all proteins (gray lines) was 1.02 **(Fig. 1H)**, indicating near-linear scaling
149 between sampled area and measured abundance. This behavior was consistent across low-,
150 medium-, and high-abundance proteins (e.g., Plxnb1, Ndufs2, and Gapdh, respectively; **Fig.
151 1H)**. In contrast, contaminants such as keratins exhibited high variability across sample sizes
152 **(Supp. Fig. 2, E-F)**, consistent with sample preparation artifacts rather than biological effects.
153 Together, these results indicate that, after accounting for contaminants, protein abundance
154 measurements scale proportionally with input material and are not detectably biased by sample
155 size.

156 Finally, we examined whether single-cell sampling selectively biases protein detection.
157 Analysis of proteins across different sample areas revealed that only 5 proteins were uniquely
158 detected in single-cell samples, whereas 182 proteins were consistently detected in all larger

159 sampled areas but absent from single-cell measurements **(Supp. Fig. S2G)**. No significant
160 functional enrichment was observed among the proteins specific to single cells. An abundance-
161 rank plot shows the distribution of these proteins **(Fig. 1I)**, with single-cell-specific proteins
162 spanning a wide dynamic range, indicating that single-cell samples can detect a broad range of
163 proteins without abundance bias. Proteins missing from single-cell samples (shown in white)
164 were predominantly low-abundance proteins, consistent with the expectation that these proteins
165 fall below detection thresholds in single-cell samples due to MS sensitivity limitations. Therefore,
166 although proteome coverage at the single-cell level remains limited by low signal-to-noise, the
167 use of DIA mitigates stochastic sampling effects relative to DDA. Collectively, these findings
168 establish LCM-based scSP as a robust and quantitatively unbiased approach for proteomic
169 characterization of individual neurons, motivating its application to biologically and spatially
170 defined neuronal populations in subsequent analyses.
171
172 **Single-cell spatial proteomics reveals region-specific neuronal proteomes**
173 We applied LCM-based scSP to characterize neuronal subtypes from distinct brain
174 regions **(Fig. 2A)**. PFA-fixed coronal brain slices from adult mice were immunostained with the
175 pan-neuronal marker anti-NeuN to enable molecularly-guided micro-dissection of single
176 neuronal cell bodies from the cortex (approximately from layers IV-V of the primary motor
177 cortex) and the substantia nigra pars compacta (SNpc) for subsequent proteomic profiling. We
178 identified approximately 2,000 proteins on average per cell (n= 40 cortex, 60 SNpc single cells;
179 **Fig. 2B**). Violin plots show comparable protein abundance CV distributions between cortex and
180 SNpc, with median CV values centered around ~50–60% in cortex and ~45–50% in SNpc, and
181 extended distribution tails reflecting the presence of highly variable proteins **(Fig. 2C)**. We
182 identified 3574 protein groups present in both neuronal populations, with an additional 85
183 proteins exclusively detected in cortical neurons and 346 in SNpc neurons **(Fig. 2D)**. Proteins
184 detected exclusively in one region may reflect biologically meaningful regional specificity. For
185 example, Icam5 and Slc6a3 (DAT), proteins known to be highly expressed in cortical neurons
186 and SNpc, respectively, were identified in the cortex-specific and SNpc-specific protein sets.
187 Unsupervised principal component analysis (PCA) revealed two distinct clusters, highlighting
188 significant molecular differences between cortical and SNpc neurons **(Fig. 2E)**. Among the 3574
189 proteins identified in both groups, 99 proteins exhibited more than two-fold upregulation in
190 cortical neurons and 345 proteins in SNpc neurons. This analysis identified multiple regionally
191 selective proteins, including Camk2a, Gria3, Homer1, and Slc17a7 in cortical neurons, whereas
192 SNpc neurons were enriched for Th, Ddc, Sncg, Calb2, Aldh1a1, and Akr1b7. To validate these

193 proteomic findings, we cross-referenced some of the identified proteins with in-situ hybridization
194 (ISH) gene expression data from the Allen Brain Atlas[24] **(Supp. Fig. 3)** and performed IF
195 validation **(Fig. 2G)**. Additionally, we plotted MS-derived intensity values, which showcase the
196 heterogeneity in protein expression at the individual cell level **(Fig. 2G)**. Together, these results
197 demonstrate that LCM-based scSP robustly resolves region-specific neuronal proteomes at
198 single-cell resolution.
199

200 **Single-cell transcriptomics informs data processing and refinement of neuronal**
201 **proteomic assignments**

202 Single-cell-level proteomics lacks standardized processing and normalization
203 workflows[25,26]. In addition to the presence of substantial missing values within datasets due to
204 the minute amount of starting material, single-cell measurements are characterized by reduced
205 signal-to-noise ratios, making quantitative comparisons particularly sensitive to pre-processing
206 strategies. To address this issue, various normalization and data imputation strategies are often
207 applied during analysis[27-29]. Here, we compared peptide-level directLFQ normalization[30] with a
208 protein-level median-based normalization strategy incorporating minimum-value imputation
209 (20% of minimum) to evaluate whether one approach performs better on single-cell spatial
210 proteomics datasets. The median-based normalization approach incorporating imputation
211 increased the number of differentially expressed proteins (DEPs) identified between cortex and
212 SNpc relative to directLFQ and produced a skewed distribution, with more proteins classified as
213 upregulated in cortex **(Fig. 3, A-B)**. However, unsupervised PCA demonstrated improved
214 separation of cortical and SNpc samples using directLFQ compared to the median-based
215 normalization approach **(Fig. 3, C-D)**. Although many established regional markers showed
216 concordant regulation across both approaches, a subset of proteins exhibited discordant
217 directionality. To resolve this conflict, we used cross-omics comparison with single-cell
218 transcriptomics datasets to assess these two normalization strategies. For this, we used the 10x
219 scRNA-seq dataset of the mouse whole-brain transcriptomic dataset from Allen Brain Atlas[31]
220 and extracted the dopaminergic neurons within the midbrain transcriptomic dataset,
221 corresponding to our SNpc proteomics cells, and IT–ET (intratelencephalic and
222 extratelencephalic) glutamatergic neurons within the MOp (primary motor cortex) dataset,
223 corresponding to our cortical proteomics cells. We observed clear separation of the cell clusters
224 and identification of region-specific enriched genes **(Supp. Fig. 4)**, some of which we also
225 identified and validated in our proteomics datasets **(Fig. 2)**.

226 We compared cortex-to-SNpc transcript ratios derived from single-cell transcriptomic
227 data with proteomic log_2 fold changes, focusing on directionality rather than effect size, as a
228 pragmatic benchmark for evaluating normalization strategies **(Supp. Table 2)**. While transcript-
229 protein correlations are known to be limited at single-cell resolution due to post-transcriptional
230 regulation, protein stability, temporal delays, and stochastic gene expression[32-34], consistent
231 regional trends across modalities provide a useful reference for assessing whether proteomic
232 processing preserves biologically plausible signal structure. Using directLFQ normalization, we
233 identified 234 gene-protein pairs with consistent up- or down-regulation and 25 pairs with
234 opposite directionality, corresponding to ~80% directional agreement and a higher correlation
235 (R^2 = 0.51). In contrast, the median-based normalization approach incorporating minimum-value
236 imputation yielded 164 same-direction and 144 opposite-direction pairs, corresponding to ~40%
237 agreement and a lower correlation (R^2 = 0.36) **(Fig. 3, E-G)**. These results highlight that
238 normalization strategy substantially influences downstream biological interpretation, and that
239 leveraging orthogonal omics data provides a principled framework for evaluating single-cell
240 proteomics processing methods. Consequently, we adopted directLFQ as the normalization
241 approach for all subsequent analyses.
242 Closer inspection of a small subset of proteins (~5.8%) that show disagreement in
243 single-cell transcriptomic directionality following directLFQ normalization **(Fig. 3G)**, revealed that
244 several corresponded to proteins of non-neuronal origin, including MBP (oligodendrocyte
245 marker) and GFAP (astrocytic marker). Because our isolation strategy relied on laser
246 microdissection rather than membrane-enclosed methods for intact single cells (i.e., cultured
247 cells or separation by cell sorting), complete exclusion of proteome contributions from
248 neighboring cells is impossible to achieve. These contaminating proteins can confound
249 investigation of cell type-specific proteomes. To systematically address this issue, we integrated
250 single-cell transcriptomic data from a publicly available Drop-seq mouse dataset (Dropviz)[35] to
251 assign a probable cellular origin to the DEPs (**Supp. Table 3**). Proteins with higher neuronal
252 transcript counts, including those exclusively detected in neurons, or with neuronal counts within
253 50% of any non-neuronal cell type (empirically defined threshold, given the LCM isolation is
254 neuron-targated) were classified as 'neuronal'. Proteins with zero neuronal transcript counts
255 were flagged as exclusively 'non-neuronal' (17 in SNpc and 6 in cortex; **Fig. 3H, left**). DEPs with
256 transcripts detected in both neuronal and non-neuronal cells, but with neuronal counts less than
257 50% of any of the non-neuronal cell types, were classified as mixed and assigned lower
258 confidence due to ambiguity in assigning cell-type origin. Interestingly, ~39% of SNpc DEPs
259 were classified as 'mixed' or 'non-neuronal', compared to ~22% for cortical DEPs, suggesting a

260 greater infiltration of one or more non-neuronal cell types within the SNpc neuronal regions
261 compared to the cortex. In 'mixed' DEPs, we observed substantial mRNA counts across multiple
262 non-neuronal cell types, including astrocytes, microglial and oligodendrocytes, preventing
263 confident assignment to a single non-neuronal class **(Fig. 3H, right)**. However, parallel IF
264 results **(Fig. 3I)** identified that astrocytes were the most disproportionately enriched non-
265 neuronal population in SNpc relative to cortex, implicating them as the primary contributor to the
266 non-neuronal component of the SNpc proteome DEP hits. Plotting the correlation of
267 transcriptomic abundance of DEPs in neurons and astrocytes further supports this (**Fig. 3J**, gray
268 area indicates DEPs of 'mixed' and 'non-neuronal' origin).
269 Taken together, these results indicate that single-cell transcriptomics can be integrated
270 with scSP both to evaluate differential expression trends across modalities and to
271 probabilistically assign cellular origin to proteomic signals, an especially critical consideration in
272 complex tissues such as the CNS. In subsequent analyses, this framework is leveraged to
273 refine cell-type attribution and biological interpretation of proteomic changes across multiple
274 spatial and cellular analyses.
275
276 **Single-cell spatial proteomics of non-neuronal cells in the CNS can capture markers of**
277 **neuroinflammation**
278 Glial cells are essential for maintaining CNS homeostasis, providing structural support,
279 regulating neuronal function, and modulating inflammatory responses[36,37]. Given their
280 importance, we next asked whether non-neuronal cell types could be reliably distinguished and
281 profiled using our approach, focusing initially on astrocytes. Brain sections were immunostained
282 with the astrocytic marker GFAP together with NeuN to enable selective isolation of non-
283 overlapping astrocyte and neuron populations **(Fig. 4A)**. Across both cell types, we identified
284 3,104 protein groups, including 185 proteins uniquely detected in astrocytes and 416 uniquely
285 detected in neurons **(Fig. 4B)**. PCA revealed cell-type-specific clustering of astrocytes and
286 neurons **(Fig. 4C)**. Differential abundance analysis identified multiple lineage-specific proteins
287 **(Fig. 4D)**: neuron-enriched proteins included Bsn, Sncb, Syn1, and Dlg4, whereas astrocyte-
288 enriched proteins included Fabp7, Vim, Anxa2, and GFAP. Integration with transcriptomic
289 datasets confirmed that neuronal DEPs corresponded predominantly to neuron-enriched
290 transcripts, while astrocyte-upregulated DEPs showed enrichment in astrocytic transcripts **(Fig.**
291 **4E)**.
292 We next applied LCM-based scSP to investigate neuroinflammation following acute brain
293 injury using a stab wound injury (SWI) model[38], which induces rapid neuronal loss along the

294 needle track and formation of a surrounding glial scar **(Fig. 4, F-G)**. GFAP^{+} astrocytes were
295 isolated from the peri-lesional region and compared with GFAP^{+} astrocytes from the
296 contralateral, uninjured hemisphere. Both groups had comparable protein counts per cell, with
297 422 proteins uniquely detected in the injured side and 512 in the uninjured side. Unsupervised
298 PCA revealed separation between injured and control astrocytes **(Supp. Fig 5, A-C)**. Proteomic
299 analysis revealed significant upregulation of proteins associated with astrocytic activation,
300 including Aldh1l1 and GFAP **(Fig. 4H)**, with increased GFAP abundance evident at the single-
301 sample level **(Fig. 4I)**.
302 Notably, acute SWI induces robust microglial activation and ramification near the injury
303 site **(Supp. Fig. 5D)**, and we detected several microglial inflammatory markers (e.g., AIF1,
304 CD68, CD11b, C1qa) in the micro-dissected astrocytic samples, which we validated via IF
305 **(Supp. Fig. 5, E-F)**, indicating that microglial populations could be amenable to LCM-based
306 scSP. We therefore attempted to profile microglia in control brain tissue using AIF1/Iba1
307 labeling. However, this proved technically challenging, likely due to the small size of microglial
308 cell bodies, necessitating methodological refinements such as thinner tissue sections and
309 reduced LCM capture areas.
310 Together, these results demonstrate that LCM-based scSP enables robust, cell-type-
311 resolved proteomic profiling of glial populations *in situ* and provides a powerful framework for
312 studying region-specific neuroinflammatory responses, including reactive gliosis, an essential
313 pathological feature of stroke, traumatic brain injury, and neurodegenerative disease.
314

315 **Proteomic profiling of Parkinson's disease-vulnerable ventral SNpc neurons reveals**
316 **basal molecular differences within closely related dopaminergic subpopulations**

317 Building on our cortex-SNpc comparison, we next asked whether LCM-based scSP
318 could resolve proteomic differences between molecularly defined neuronal populations that are
319 highly similar in anatomy and function and inaccessible to bulk approaches. We focused on
320 dorsal and ventral neuronal subpopulations of SNpc, the latter of which selectively degenerate
321 in PD[4,39]. To isolate these populations, we employed dual immunostaining for TH to label SNpc
322 dopaminergic neurons and annexin A1 (Anxa1) to selectively mark the ventral tier population[40],
323 enabling comparison of TH^{+}/Anxa1^{+} ventral neurons with TH^{+}/Anxa1^{-} dorsal neurons **(Fig. 5A)**.
324 We identified 3,370 protein groups common to both Anxa1^{+} and Anxa1^{-} neurons, with an
325 additional 126 proteins uniquely detected in Anxa1^{+} neurons and 225 uniquely detected in
326 Anxa1^{-} neurons (n = 15–17 single neurons per group; **Fig. 5B**). PCA failed to robustly separate
327 the two populations, possibly due to their anatomical and functional proximity **(Fig. 5C)**.

328 Therefore, we used relaxed statistical thresholds ($p < 0.1$, FC ≥ 1.5) to identify 370 proteins
329 significantly upregulated in Anxa1^{+} neurons and 189 enriched in Anxa1^{-} neurons **(Fig. 5D)**. The
330 dataset was enriched for canonical neuronal proteins, including synaptic, cytoskeletal, and
331 neurotransmission-related markers such as Map2, Camk2a, Th, Stmn3, Vamp1, Cadps2, Calb1,
332 and Aldh1a1, confirming neuronal identity at the proteomic level. Within the neuronal proteome,
333 Anxa1 itself was differentially regulated, as expected **(Fig. 5E)**. Notably, Aldh1a1 was enriched
334 in ventral-tier neurons, whereas Calb1 was elevated in dorsal-tier neurons; these proteins have
335 been previously implicated in dopamine metabolism and calcium homeostasis, respectively, and
336 could be associated with differential vulnerability of SNpc subpopulations **(Fig. 5E)**. These
337 findings were validated by IF **(Fig. 5F, Supp. Fig. 6)** and are consistent with prior trascriptomics
338 reports[40,41]. Together, these results demonstrate that LCM-based scSP can resolve subtle yet
339 biologically meaningful proteomic differences between closely related neuronal subpopulations,
340 providing complementary insight to transcriptomic approaches[42] for dissecting cell type-specific
341 mechanisms underlying selective neuronal vulnerability in PD and related disorders.
342

343 **Single-cell spatial proteomics identifies proteins and pathways altered in pS129-αSyn**
344 **inclusion-bearing neurons in a murine model of Parkinson's disease**

345 Deciphering molecular-level insights selectively from the small, spatially restricted
346 neuronal populations that harbor pathogenic protein inclusions in neurodegenerative disorders
347 such as PD remains challenging. For example, in human post-mortem samples from patients
348 with PD or dementia with Lewy bodies, only ~1-2% of neurons contain mature Lewy bodies[3],
349 and even in inducible murine models, inclusion-bearing neurons typically comprise only a
350 fraction of the local SNpc population[43]. A recent study used spatial transcriptomics to map
351 molecular alterations in pathology-enriched brain regions[44]; however, proteomic changes at the
352 single-cell level have not been investigated. To address this, we applied LCM-based scSP to a
353 murine model of PD, modeling the symptomatic stage of parkinsonism using direct injection of
354 pathogenic αSyn preformed fibrils (PFFs)[45-47]. Adult C57 mice received intrastriatal injections of
355 sonicated mouse PFFs, and brain tissue was collected 6 months later. IHC confirmed αSyn
356 aggregates marked by pS129-αSyn in a fraction of surviving SNpc neurons **(Fig. 6A)**, and these
357 inclusions also stained positive for canonical pathology markers such as ubiquitin and p62
358 **(Supp. Fig. 7)**.
359 Aggregate-containing (Agg^{+}) and non-aggregate-containing (Agg^{-}) neurons **(Fig. 6A)**
360 were laser-captured from PFF-injected mice nigral tissue dual-labeled for a dopaminergic

361 marker (TH) and anti-pS129-αSyn antibody, with non-aggregate neurons collected from the
362 PBS-injected contralateral control side of the same animals. On average, we detected ~2,000
363 unique proteins per individual neuron **(Fig. 6B)** and ~4300 protein groups across both neuronal
364 populations, with 703 proteins exclusive to Agg^{-} neurons and 214 proteins to Agg^{+} neurons
365 **(Fig. 6C)**. Unsupervised dimensionality reduction resolved the two neuronal groups into distinct
366 clusters, with Agg^{+} neurons showing markedly higher variability **(Fig. 6D)**. Analysis of DEPs
367 **(Fig. 6E)** and pathway enrichment analysis of the DEPs using KEGG, a curated compendium of
368 experimentally validated molecular networks[48], revealed strong overrepresentation of pathways
369 related to "Parkinson's disease," "Oxidative phosphorylation," "Metabolic pathways," and the
370 "Ribosome" **(Fig. 6F)**. Consistently, gene ontology enrichment across cellular components,
371 molecular functions, and biological processes yielded overlapping categories **(Supp. Fig. 8)**.
372 Mapping the altered proteins onto the KEGG Parkinson's disease pathway highlighted multiple
373 nodes along established pathogenic routes **(Supp. Fig. 9)**. Dysregulation of the ubiquitin-
374 proteasome system was evident, marked by increased abundance of several proteasomal
375 subunits (e.g., PSMB5, PSMA7) in Agg^{+} neurons together with reduced levels of the familial PD-
376 linked deubiquitinase UCHL1 **(Fig. 6G)**. Mitochondrial dysfunction also emerged prominently,
377 reflected by widespread downregulation of subunits from respiratory chain complexes I-V.
378 Notably, numerous ribosomal proteins (RPL and RPS families) were decreased in Agg^{+}
379 neurons. Network analysis further identified a connected module of ribosome-associated RNA-
380 binding proteins, including several spliceosome components **(Supp. Fig. 10)**, suggesting
381 coordinated perturbation of translational and RNA-processing machinery. These results support
382 multi-pathway alterations in αSyn aggregate-containing neurons in this model of Parkinsonism.
383 Together, these findings illustrate how LCM-based scSP enables proteome-wide
384 interrogation of rare, pathology-defined neuronal subpopulations *in vivo*, offering a powerful
385 framework to single-cell resolution analysis of proteomic states associated with
386 neurodegenerative diseases.

387 **Discussion**

388 Laser capture microdissection-based spatial proteomics has emerged as a key method
389 for studying complex biological systems, enabling interrogation of deep proteomic complexity
390 while preserving tissue context[49,50]. To date, spatial proteomics at the single-cell level has only
391 been applied to peripheral somatic tissues with comparatively lower cellular diversity or spatial
392 complexity[19,51], and application to the brain remains challenging due to its cellular and
393 architectural complexity. Here, we apply LCM-based single-cell spatial proteomics (scSP) to
394 multiple neuroscience use cases, demonstrating its performance as an unbiased, discovery-
395 oriented platform for single-cell proteomic analysis of the nervous system. We show that
396 molecularly-guided spatial proteomics enables robust and quantitative profiling of CNS cells
397 across sample fixation conditions, staining modalities, and sampling area, extending to the
398 single-cell regime. A key methodological advantage of this approach is its compatibility with
399 established imaging modalities, including protein-based IF and mRNA-based FISH **(Fig. 1C-D,**
400 **Supp. Fig. 1B-C)**. Large-scale transcriptomic studies have established mRNA expression as a
401 robust cell-type marker, and in some cases, such as for synaptically localized proteins (e.g.,
402 GAD1 in inhibitory neurons), mRNA-based labeling more effectively visualizes neuronal cell
403 bodies than antibody staining, which often preferentially labels distal processes. Using this
404 framework, we successfully resolved brain region-specific neuronal populations **(Fig. 2E)** and
405 identified multiple high-confidence cell-type-specific protein markers **(Fig. 2, Supp. Fig. 4)**,
406 supported by orthogonal histological and transcriptomic ISH evidence.

407 The increasing availability of well-annotated large-scale single-cell transcriptomic
408 atlases, particularly for mouse and human brain[24,52], provides a valuable and accessible
409 resource for comparative multi-omics analyses and validation. These atlases can also enable
410 evaluation of analytical strategies in single-cell proteomics. In this study, we leveraged
411 transcriptomic data to assess the impact of different protein data processing approaches and
412 observed that directLFQ-based normalization substantially improved agreement with
413 transcriptomic trends compared to commonly used global imputation and median normalization
414 strategies in these sparse, tissue-derived single-cell conditions **(Fig. 3, A-G).** Moreover, we
415 used transcriptomics to assign confidence in cell-type origin of proteomics hits **(Fig. 3, J, Supp.**
416 **Fig. 4)**. This refinement is particularly important in heterogeneous tissues such as the brain,
417 where low-input spatial sampling can capture proteins originating from neighboring or
418 intermingled cells and processes. Together, these observations highlight the potential of
419 transcriptomics-informed comparisons as a pragmatic means of benchmarking and refining
420 single-cell proteomics analysis pipelines. Incomplete concordance between transcriptomic and

421 proteomic measurements, consistent with prior studies[34,53,54], underscores the complementary
422 nature of the two modalities and highlights opportunities for insights from proteomics that are
423 not accessible through transcriptomics alone.
424 Analysis of neuroimmune responses in the stab wound injury (SWI) model provided
425 additional methodological insights into integrating proteomic and transcriptomic data analyses.
426 We observed substantial overlap between our proteomic hits and a recent SWI transcriptomic
427 study[38], with comparable fold changes for most shared targets, including Anxa3, B2m, Dhrs1,
428 S100a6, Npl, Ptpn6, Isg15, C1qa, and C1qc. In contrast, CD68, a key inflammatory marker,
429 showed greater enrichment at the protein level (~6-fold) **(Supp. Fig. S5F)** in our dataset
430 compared to transcriptomic measurements (~2.5-fold). This disparity likely reflects localized
431 accumulation of CD68 protein near the stab wound injury axis, from which our samples were
432 collected, whereas corresponding mRNA signals are more spatially diffused, as reported
433 previously[38]. Consistent with this, spatial imaging of selected targets in the same study revealed
434 pronounced differences between mRNA and protein localization, further reinforcing that
435 transcriptomic and proteomic measurements provide complementary, rather than
436 interchangeable, information.
437 Together, these findings highlight the depth and specificity enabled by LCM-based
438 molecularly-guided scSP, positioning this approach as a powerful framework for studying
439 neurodegenerative diseases such as PD, where selective neuronal vulnerability and sparse,
440 mosaic pathology pose persistent challenges to mechanistic understanding. Although SNpc
441 neuronal subtypes have been extensively characterized at the transcriptomic level[42], their
442 proteomic organization and its relationship to vulnerability remain largely unexplored. Our
443 analysis reveals many proteomic differences between ventral and dorsal SNpc neurons,
444 including alterations in proteins related to dopamine oxidation[55], such as Aldh1a1 (**Fig. 5, E–F**),
445 suggesting proteomic specializations that may contribute to differential susceptibility, although
446 further work will be required to define the underlying mechanisms.
447 Within our dataset examining proteomic changes in sparsely populated, aggregate-
448 containing neurons, we observed enrichment of gene ontology terms (**Supp. Fig. 8**) and KEGG
449 pathways (**Supp. Fig. 9**) associated with PD in aggregate-associated differentially expressed
450 proteins (DEPs), supporting the biological robustness of the dataset. These DEPs pointed
451 toward coordinated disruption of proteasomal and mitochondrial pathways (**Fig. 6G**), reflected
452 by widespread alterations in their core subunits, two systems that represent central mechanistic
453 pillars of PD biology[56]. Aggregated αSyn is known to impair proteasomal degradation
454 (McNaught and Jenner 2001, Thibaudeau, Anderson et al. 2018) and directly interacts with

455 mitochondrial membranes[57,58], leading to respiratory dysfunction. Consistent with this, we
456 observed reduced levels of the PD-associated deubiquitinase Uchl1[59], indicative of sustained
457 proteostasis failure. Similar proteasomal and mitochondrial alterations were also detected in
458 single-cell proteomics data from an orthogonal PFF-induced PD model in the regenerative spiny
459 mouse[60], suggesting these responses possibly represent conserved features of αSyn pathology.
460 In parallel, we detected reduced abundance of multiple ribosomal proteins, indicating
461 compromised translational capacity. This aligns with prior reports of ribosomal dysfunction and
462 clinical observations of reduced RPL and RPS subunits in PD patient brains[61,62], although these
463 studies were conducted at the bulk tissue level. Together, the combined disruption of translation
464 and ubiquitin–proteasome function suggests a potential decoupling between transcript
465 abundance and protein clearance, underscoring the importance of proteomic analyses for
466 accurately defining neuronal state in PD.

467 Several previous studies have characterized proteomic alterations in PD patient tissue
468 and preclinical models using bulk approaches[63-65]. Bulk and single-cell approaches may exhibit
469 pathway-level convergence; however, the specific proteins underlying these signatures can
470 differ. For example, direct comparison of our DEPs with a recent bulk proteomic study[63] using a
471 similar experimental paradigm revealed limited overlap, likely reflecting the whole-tissue nature
472 of bulk analysis. In contrast, a more substantial overlap was observed with human Lewy body
473 interactor proteins reported by Killinger et al.[66], providing validation of our neuron-enriched
474 readouts, given that Lewy bodies are restricted to neurons in PD patients. The limited
475 concordance with bulk datasets is consistent with the inherent non-specificity of whole-tissue
476 measurements, including contributions from non-neuronal cell types and dilution of disease-
477 relevant signals in tissues where pathology is confined to a subset of 1-2% neurons[3]. By
478 resolving proteomes at the level of individual dopaminergic neurons, our single-neuron analysis
479 overcomes limitations from tissue-averaged measurements. Notably, dimensionality-reduction
480 analysis (**Fig. 6D**) revealed a compact cluster of aggregate-free neurons, whereas aggregate-
481 containing neurons exhibited substantial divergence, suggesting heterogeneous stress
482 responses elicited by αSyn pathology that are only resolvable through single-cell approaches
483 and further highlighting the scope of scSP.

484 Several limitations of the LCM-based scSP approach should be considered, particularly
485 when applied to the brain. First, the complex and intermingled architecture of the brain can lead
486 to proteomic contamination. For example, we detected astrocytic proteins in SNpc neuronal
487 samples **(Fig. 2, Fig. 5)**, and microglial proteins in isolated ramified astrocytes in SWI samples
488 **(Fig. 4, Supp. Fig. 5, D-F)**. Contaminating proteins may also originate from closely related cell

489 types, such as different neuronal subpopulations. For instance, in our dopaminergic subtype
490 analysis, Anxa⁻ samples showed significant non-zero proteomic intensity values for Anxa1 **(Fig.**
491 **5E)**, unlike the near-zero expression levels of SNpc markers such as TH or Sncg in spatially
492 separated cortical samples **(Fig. 2G)**. This is notable given prior transcriptomic analyses[40] and
493 IF imaging indicating that Anxa⁻ SNpc neurons exhibit undetectable (not just low) Anxa1
494 expression **(Fig. 5A, 5F)**. Such effects likely arise from overlapping cells or processes within the
495 target ROI, particularly along the Z-axis, where precise isolation of neuronal cell bodies is
496 inherently challenging. Related to this, proteins predominantly localized to neuronal processes
497 or synapses are underrepresented in single-cell samples compared to larger ROI samples
498 reflecting an intrinsic limitation of cell-body based isolation strategies for cells with complex
499 structures.

500 Second, sample variability remains a challenge; high coefficient of variations (CVs) and
501 missing values were observed, as is typical for single-cell studies[26,67]. This is particularly
502 important when distinguishing biological or disease-specific differences from variability
503 introduced by methodological heterogeneity. To improve downstream biological interpretability,
504 we purposefully omitted features not present in at least 40% of samples in at least one group
505 (see Methods). While small sample sizes can therefore be sufficient to detect protein differences
506 with large effect sizes (e.g., **Fig. 4**), especially given histology-guided rather than blind isolation
507 of cells, larger sample sizes will likely be required to resolve more subtle differences.

508 In contexts where cell-specific heterogeneity is driven by biological factors or disease
509 states, disentangling these limitations from technical variability is a challenge, underscoring the
510 need to balance sensitivity and interpretability. Ongoing advances in MS sensitivity, reduced
511 costs for single-cell processing, and continued methodological and analytical improvements in
512 LCM are expected to further enhance the utility of LCM-based scSP for CNS studies. In this
513 study, as discussed above, integration with orthogonal transcriptomic datasets provided
514 additional context to distinguish biologically meaningful heterogeneity from low-input or technical
515 effects. In addition, although not applied here, machine learning-based strategies, such as those
516 used in deep visual proteomics[19,21,49,68], could further improve cell selection by minimizing
517 overlap among histology-positive neurons and enhancing cell annotation throughput.

518 In summary, this work establishes single-cell spatial proteomics (scSP) as a powerful
519 approach for studying the nervous system, enabling investigation of diverse biological questions
520 and disease states, and provides a foundation for continued technical and analytical refinement.

521 **Materials and Methods**

522 **Post-mortem tissue processing:** All mouse procedures were approved by the
523 Institutional Animal Care and Use Committee (IACUC) at the California Institute of Technology.
524 Animals were euthanized using a sodium pentobarbital overdose and subjected to transcardial
525 perfusion with chilled PBS. Brains were either collected and flash frozen using a dry ice-ethanol
526 bath, or perfusion was continued with 4% (w/v) paraformaldehyde (PFA) in PBS to fix the brain.
527 Fixed brains were then collected and kept for 24-48 hr in PFA solution and subsequently
528 cryoprotected at 4°C in a solution containing 30% (w/v) sucrose for 72 hr. Brains were flash-
529 frozen in O.C.T. Compound (Scigen, #4586) using a dry ice-ethanol bath and kept at -70 °C until
530 sectioning. Brain sections were obtained using a cryostat (Leica Biosystems) and collected in 1x
531 PBS. Sections were stored at 4ºC in PBS (supplemented with 0.02% Azide) for short-term
532 storage or at - 20ºC in cryoprotectant (Bioenno Lifesciences, 006799-1L) for longer
533 preservation. Detailed protocol available at 10.17504/protocols.io.14egn1j4yv5d/v1.

534 **Mouse αSyn PFF preparation:** Recombinant mouse αSyn PFFs were produced as
535 previously outlined[60]. In summary, αSyn monomer was produced in E. coli BL21 (DE3) cells
536 utilizing the pT7-7 vector and subsequently purified through size-exclusion chromatography
537 (Cytiva) and anion-exchange chromatography on a HiPrep Q HP 16/10 column (Cytiva).
538 Endotoxin was eliminated using endotoxin-reduction resin (Thermo Fisher Scientific, #88277),
539 resulting in preparations with <0.02 EU/µg. Monomeric αSyn (5 mg/mL in PBS) was filter
540 sterilized with a 0.22 µm filter and incubated at 37 °C with continuous agitation at 1,000 rpm to
541 facilitate fibril formation. Following the elimination of remaining monomer via centrifugation, the
542 resultant fibrils were resuspended in PBS at a concentration of 5 mg/mL, aliquoted into 25 µL
543 portions, and preserved at –80 °C. Prior to injection, fibrils were sonicated with a cup-horn
544 sonicator (Qsonica Q700) to generate short PFF fragments suitable for *in vivo* seeding. Detailed
545 protocol available at 10.17504/protocols.io.14egn1j4yv5d/v1.

546 **Intracranial stereotaxic surgery**: Mice were group housed under controlled conditions,
547 maintained on a 13/11-hour light/dark cycle at ambient temperatures ranging from 71 to 75°F,
548 with humidity levels between 30% and 70%. Stereotaxic surgery was performed as described
549 previously [60]. Before surgery, animals were anesthetized using isoflurane, and the animal was
550 secured on the stereotaxic frame (Kopf Instruments). For the stab wound injury (SWI)
551 experiment, a needle tip (26 gauge) insertion was performed at the coordinates 0.25 AP, -2 ML,
552 -3 DV and left in place for 5 minutes. For PFF injection, 1.5uL of 5mg/mL sonicated PFF was
553 injected at the coordinates 0.25 AP, -2 ML, -3 DV and PBS was injected into the contralateral
554 hemisphere of the same animal as a control. Following the injection, the scalp was closed using

non-absorbable nylon sutures (Ethicon #NW3353). Animals were allowed to recover on a heating pad and monitored for health concerns regularly for the next few days. SWI and PFF-injected animals were culled 7 days and 24 weeks post-injection, respectively, to collect the brain as described above. Detailed protocol available at 10.17504/protocols.io.14egn1j4yv5d/v1.

Immunofluorescence (IF) staining: For IF staining, 30 µm or 35 µm (**Supp. Fig. 1, B,D**) free-floating brain sections were blocked with 10% (v/v) normal donkey serum in PBS supplemented with 1% Triton-X100 (% v/v) (1% PBST) for 90 min and then incubated with primary antibody solution prepared in 0.3% PBST supplemented with 1% (v/v) normal donkey serum overnight at 4°C. After washing in PBS (3 x 10 min), the sections were incubated with secondary antibodies (in 0.3% PBST with 1% NDS) conjugated with Alexa fluorophores (Jackson ImmunoResearch Laboratories, 1:500 dilution) for 90 min at room temperature and then washed 3 x 10 min in PBS. The tissues were mounted on glass slides or UV-treated metal frame slides with PET membranes (Leica Microsystems, #76463-322) for confocal imaging and laser capture microdissection, respectively. Glass slides were allowed to dry overnight and sealed with a coverslip using mounting media (Thermo Fisher Scientific, #P36970). The following primary antibodies were used for IF staining: anti-tyrosine hydroxylase (EMD Millipore, # AB152, RRID:AB_390204, 1:1000; #MAB318, RRID:AB_2313764, 1:1000); anti-GFAP (Abcam, #ab4674, RRID:AB_304558, 1:1000), anti-Iba1 (FUJIFILM Wako Pure Chemical Corporation, #019-19741, RRID:AB_839504, 1:1000), anti-CD11b (Thermo Fisher Scientific, RRID:AB_467108, #14-0112-82, 1:500), anti-CD68 (Thermo Fisher Scientific, RRID:AB_11151139, #14-0688-82, 1:500), anti-NeuN (Cell Signaling Technology, #94403, RRID:AB_2904530, 1:1000; Abcam, #ab104224, RRID:AB_10711040, 1:1000) , anti-Anxa1(Thermo Fisher Scientific, #71-3400, RRID:AB_2533983, 1:250), anti-Aldh1a1 (Thermo Fisher Scientific, #PA5-17943, RRID:AB_10977372, 1:250), anti-Calb1 (Swanth, #CB38a-200uL, RRID:AB_3107026, 1:500), anti-gamma-synuclein (Genetex, #GTX110483, 1951959, 1:500), anti-Camk2a (Abcam, #ab52476, RRID:AB_868641, 1:500), anti-pSer129-αSyn (EP1536Y) (Abcam, #ab51253, RRID:AB_869973, 1:500), anti-Ubiquitin (Proteintech, #80992-1-RR, RRID:AB_2923694, 1:500), anti-p62/SQSTM1 (Proteintech, #18420-1-AP, RRID:AB_10694431, 1:500). Detailed protocol available at 10.17504/protocols.io.14egn1j4yv5d/v1.

Hybridization chain reaction (HCR): Split initiator probes[69] against *Itpr1, Gad1*, and *Gad2* were designed **(Supp. Table 4)** according to Jang *et al.*[70] and ordered from Integrated DNA Technologies. All washes and incubations were performed at room temperature and with gentle shaking unless otherwise stated. All wash and incubation buffers were prepared from

589 RNase-free reagents. Free-floating sections of the mouse brain were permeabilized in 1x PBS
590 with 0.1% Triton-X100 for 1 hr. Sections were then incubated for 1 hr at 37 °C in a probe
591 hybridization buffer consisting of 2x SSC, 10 % ethylene carbonate (Sigma-Aldrich, #E26258),
592 and 10% dextran sulfate (Sigma-Aldrich, #3730). Following equilibration in hybridization buffer,
593 the samples were incubated for 16 hr at 37 °C in pre-warmed fresh hybridization buffer plus 2
594 nM of each probe. After probe hybridization, sections were washed twice for 30 min in stringent
595 wash buffer (2x SSC, 30% ethylene carbonate) at 37 °C, then twice for 30 min in 5x SSC with
596 0.1 % Tween-20 (Sigma-Aldrich, #P1379), and then incubated in HCR amplification buffer (2x
597 SSC, 10% ethylene carbonate) for 1 hr. Alexa Fluor 647 or 488-conjugated hairpins (Molecular
598 Technologies) were heated to 95 °C for 90 s, then cooled to room temperature for 30 min in the
599 dark. Following equilibration in amplification buffer, the tissue was incubated in amplification
600 buffer with 60 nM hairpins for 16 hr. After HCR amplification, the samples were washed twice for
601 30 min each in 5x SSC with 0.1 % Tween-20, followed by two washes in 1x PBS for 10 min.
602 Sections were stored in 1x PBS at 4 °C until use. Detailed protocol available at
603 10.17504/protocols.io.14egn1j4yv5d/v1.

604 **Confocal Imaging:** Images were acquired using (i) a spinning disk confocal microscope
605 (Andor, Oxford Instruments), using a 10x, 0.30 NA air objective or 25x, 0.95 NA water-
606 immersion objective, operated with Fusion software (v2.3.0.44) and visualized using Imaris
607 software(v9.5.1, Oxford Instruments, RRID: SCR_007370) and (ii) a Zeiss LSM 880 (Zeiss),
608 using a 25x, 0.8 NA water-immersion objective or 10x, 0.45 NA air objective, operated with Zen
609 Black (v2.3) and visualized using Zen Blue (v2.5).

610 **Laser-capture micro-dissection (LCM):** Regions of interest were mounted on PET
611 membranes (Leica Microsystems, #76463-322) and excised using a gravity-driven collection
612 system by a Leica LMD7000 and LMD7. Laser settings are included in **Supp. Table 5**. The cut
613 tissue was collected in a 0.65 mL Low Binding Tube cap (Sorenson SafeSeal, #11300;
614 Eppendorf LoBind, # 0030108434) containing 10 µL of lysis buffer consisting of 50 mM
615 triethylammonium bicarbonate (TEAB) (Thermo Scientific, #90114) and 0.2% n-Dodecyl-beta-
616 Maltoside (DDM) (Thermo Scientific, #89903). Upon collecting, the tube was vortexed upside
617 down for 30 seconds and centrifuged at 13,000 x g for 1 minute at 25°C. The sample was then
618 stored at -80°C until further processing. Detailed protocol available at
619 10.17504/protocols.io.14egn1j4yv5d/v1.

620 **Sample preparation for mass spectrometry:** Stored samples were thawed and
621 vortexed for 30 seconds in an inverted position with an additional 10 µL of lysis buffer to ensure
622 optimal recovery of the tissue. The sample was then centrifuged at 13,000 x g for 1 minute at

623 25°C and transferred into a LoBind 384-well PCR plate (Eppendorf, #0030129547). The plate
624 was heated for two hours at 70°C in a QuantStudio™ Real-Time PCR machine with the heated
625 lid set to 85°C for sample lysis and protein denaturation. Following lysis, the plate was
626 centrifuged at 1000 x g for 1 minute and allowed to cool to room temperature. Proteolytic
627 digestion was carried out using a mix of trypsin (Promega, #V5280) and Lys-C (Wako
628 Chemicals, # 125-05061). 1 µL of the digestion mix containing 4 ng of each enzyme was added
629 to each sample. The plate was then incubated at 37°C overnight. Following digestion, samples
630 were centrifuged at 1000 x g for one minute, and digestion was quenched with 0.5 µL of
631 aqueous buffer comprising 2% acetonitrile and 4% formic acid. Detailed protocol available at
632 10.17504/protocols.io.14egn1j4yv5d/v1.

633 **LC-MS/MS analysis**: Peptides were separated on an Aurora Ultimate UHPLC Column
634 (25cm by 75µm, 1.7µm C18, AUR3-25075C18, IonOpticks) with column temperature maintained
635 at 50°C. 5 µL of each sample was loaded directly onto the analytical column to maximize
636 sensitivity. The LC system (Vanquish Neo UHPLC, Thermo Scientific) was coupled to an
637 Orbitrap Exploris 480 mass spectrometer (Thermo Scientific) with a Nanospray Flex ion source
638 (Thermo Scientific). Peptides were separated using a 60-min gradient at a flow rate of 0.22
639 µL/min.

640 For αSyn aggregate-bearing SNpc neurons, the same LC system was coupled to an
641 Orbitrap Astral mass spectrometer (Thermo Scientific) equipped with an EasySpray ion source,
642 with the column maintained at 55°C. These samples were analyzed using a 19.5-min gradient at
643 a flow rate of 0.2 µL/min. Detailed LC gradients for both platforms are provided in the **Supp.**
644 **Table 6**.

645 Xcalibur software (Thermo Scientific) was used for method implementation and data
646 acquisition on both mass spectrometers. Data-dependent acquisition (DDA) on the Orbitrap
647 Exploris 480 was performed in positive ion mode (spray voltage 1.6 kV, ion transfer tube at
648 300°C). Full MS1 scans were acquired over a m/z range of 375-1200 at a resolution of 60,000
649 with a cycle time of 3 seconds. The maximum injection time was set to auto, and the normalized
650 AGC target was set to 300%. Precursor ions with charges ranging from +2 to +6 were
651 selectively targeted for fragmentation using a minimum intensity threshold of 5e3. Dynamic
652 exclusion was set to exclude after one acquisition, with a 45-second exclusion duration and 10
653 ppm mass tolerance. MS2 scans were acquired in the Orbitrap at 60,000 resolutions with an
654 isolation window of 1.6 m/z, HCD collision energy set at 28%, and an auto-adjusted maximum
655 injection time. The normalized AGC target was set at 200%.

656 Data-independent acquisition (DIA) on the Orbitrap Exploris 480 was performed in
657 positive ion mode (spray voltage 1.6 kV, ion transfer tube at 300°C) using parameters adapted
658 from Matzinger *et al.*[23]. Briefly, MS1 full scans were acquired with a range of 375-1200 m/z and
659 a resolution of 120,000. The maximum injection time was set to auto, and the normalized AGC
660 target was set to 300%. MS2 scans were acquired at 60,000 resolutions with a maximum
661 injection time of 118 ms and AGC target of 75%.
662 For the Orbitrap Astral, DIA was performed in positive ion mode (spray voltage 1.8 kV,
663 ion transfer tube at 275 °C). MS1 spectra were acquired at 240,000 resolution across a scan
664 range of 400-800 m/z with an injection time and an AGC target of 500%. MS2 spectra were
665 acquired on the Astral analyzer with an 80-ms injection time and an AGC target of 800%.
666 Comprehensive DDA/DIA parameters and mass spectrometer settings for both mass
667 spectrometers are listed in the **Supp. Table 6**. Detailed protocol available at
668 10.17504/protocols.io.14egn1j4yv5d/v1.
669 **Mass spectrometry data analysis and statistics:** RAW files obtained in DDA mode
670 were processed in Proteome Discoverer 2.5 (Thermo Fisher Scientific) using the SequestHT[71]
671 search algorithm with Percolator validation. Data was searched against the mouse reference
672 database from Uniprot (SwissProt database, downloaded 27 September 2024, 17232
673 sequences). Lys-C and Trypsin were selected, allowing for a maximum of two missed cleavages
674 and peptide lengths between seven and 30 amino acids. The mass tolerance for precursor ions
675 was set at 20 ppm, while the fragment mass tolerance was defined as 0.1 Da. INFERYS
676 Rescoring was used in automatic mode, and Percolator was used for search validation based
677 on q-values with a strict false discovery rate (FDR) of 1% at the spectrum level[72,73].
678 Carbamidomethylation of cysteine residues was designated as a static modification, and
679 oxidation of methionine residues was considered a dynamic modification. A minimum number of
680 1 peptide sequence (unique and razor) was required for protein identification. Strict parsimony
681 was used to group proteins. Data was exported from PD2.5 and used for further analysis.
682 RAW files acquired in DIA mode were processed with DIA-NN (version 2.1) [74] using a
683 library-free search with FASTA digest enabled and deep learning–based predictions for spectra
684 and retention times. Default DIA-NN parameters were used unless otherwise specified, with the
685 precursor *m/z* range restricted to 400–800 and a maximum of two missed cleavages allowed.
686 Precursor FDR cutoff was set to 1.0%. Resulting protein- and peptide-level outputs (in parquet
687 format) were imported into Python for downstream analysis using single-cell analysis packages
688 *scanpy*[75] and *scpviz*[76], with additional analysis and visualization performed using general-
689 purpose scientific Python libraries documented in the repository README **(Supp. Table 1)**.

690 Proteins meeting a stringent confidence threshold (PG.Q.Value < 0.01) were designated as high
691 confidence and retained for subsequent analyses. Additional filtering required proteins to be
692 quantified in at least 40% of samples within at least one group per comparison (e.g., region or
693 condition). Proteins lacking valid gene annotations or exhibiting non-unique abundance profiles
694 were excluded, as isoform-level redundancy combined with sparse peptide support resulted in
695 unreliable quantification. Protein abundances were normalized using directLFQ[30] which was
696 adopted as the primary normalization strategy. For comparison, an alternative normalization
697 approach involving global imputation to 20% of the minimum observed intensity followed by
698 median normalization was evaluated but not used for downstream analyses. Statistical analysis,
699 sample clustering based on principal component analysis, and volcano plots were generated
700 utilizing scpviz. Kolmogorov-Smirnov (KS) normality test was used to test the distribution for
701 whether proteins unique to certain conditions lay within the original sample distribution (rank plot
702 shown in Fig. 1I). Differences in mean protein and peptide counts between conditions were
703 evaluated using Student's *t*-test. Protein abundance was plotted using GraphPad Prism (v9.5.1,
704 http://www.graphpad.com, RRID: SCR_002798).

705 **Transcriptomics data analysis and multi-omics comparison:** Single-cell RNA
706 sequencing (scRNA-seq) data were obtained from the Allen Brain Cell Atlas mouse whole-brain
707 cell-type atlas (10x Genomics v3) [24,31]. Data processing and quality control were performed as
708 previously described by Yao et al.[31], including stringent filtering based on gene detection
709 thresholds, quality control metrics, and doublet scores. The resulting curated scRNA-seq
710 datasets were used directly for downstream analyses. Processed datasets from WMB-10Xv3-
711 Isocortex-1, WMB-10Xv3-Isocortex-2, and WMB-10Xv3-MB were combined, with cells selected
712 based on supertype annotations corresponding to cortical ("CTX") and midbrain dopaminergic
713 populations ("*-VTA"). Additional filtering retained cells whose region-of-interest acronyms
714 matched MOp (motor cortex) or MB (midbrain). Cells annotated as "L5 NP CTX Glut" and "SNr"
715 were excluded, as these populations do not correspond to the neuronal subtypes analyzed in
716 the proteomics experiments. Regions were annotated by mapping MOp to cortex and MB to
717 SNpc. Transcriptomic data were converted to AnnData format and analyzed using Scanpy,
718 including dimensionality reduction and visualization using uniform manifold approximation and
719 projection (UMAP).

720 For multi-omics analysis, proteomics data were imported and processed using scpviz as
721 described above. The protein-level AnnData object (.prot) from the pAnnData structure was
722 used to enable direct integration with transcriptomic analyses. Differentially expressed proteins
723 (DEPs) and genes were identified using a fold-change threshold of at least two and a

724 significance cutoff of $p < 0.05$ based on Student's t-test. Concordance between transcriptomic
725 and proteomic changes was assessed by comparing the directionality of differential expression,
726 categorizing features as consistently upregulated, consistently downregulated, or oppositely
727 regulated across the two modalities.
728 To assess the cell-type origin of DEPs, we queried corresponding genes against Drop-
729 seq transcriptomic datasets using the DropViz portal. DEP gene lists were entered as query
730 genes, and the relevant brain region was selected as either the frontal cortex or substantia
731 nigra, as appropriate. Major cell classes were preselected, including astrocytes, neurons,
732 oligodendrocytes, endothelial cells, and microglia/macrophages. When multiple clusters were
733 present within a given cell class, the cluster most relevant to the experimental context was
734 selected (e.g., SN Neuron_Th [#4] for SNpc dopaminergic neurons and FC
735 Neuron_Layer5_Parm1 [#7] for cortical neurons). Natural log–transformed expression values
736 were extracted and plotted in correlation plots using GraphPad Prism.
737 **Bioinformatics and enrichment analyses:** Gene ontology (GO) analysis comparing
738 fixed and frozen tissue was performed using string-db[77]. For the αSyn PFF experiment, pathway
739 enrichment analysis was conducted using ShinyGO (v0.85.1;
740 http://bioinformatics.sdstate.edu/go/, RRID:SCR_019213) with Kyoto Encyclopedia of Genes
741 and Genomes (KEGG; http://www.kegg.jp, RRID:SCR_012773) as the reference database.
742 Analyses were performed for mouse genes (GRCm39), applying an FDR cutoff of 0.05, pathway
743 size limits of 5–5,000 genes, and reporting the top 10 enriched pathways. Enrichment results
744 were visualized as hierarchical enrichment trees and KEGG pathway maps.
745 GO enrichment analysis was additionally performed using Metascape (https://metascape.org,
746 RRID:SCR_016620), with annotations spanning biological process (BP), molecular function
747 (MF), and cellular component (CC). Enrichment was assessed using a minimum overlap of
748 three genes, a P-value cutoff of 0.01, and all genes as background. GO term visualization was
749 carried out using Cytoscape (v3.10.3; https://cytoscape.org, RRID:SCR_003032).
750 Protein–protein interaction (PPI) networks were generated using STRING (https://string-db.org,
751 RRID:SCR_005223), using the full STRING network with experimentally supported interactions
752 only, highest confidence threshold (0.9), and MCL clustering.

Figures and figure legends

Figure 1

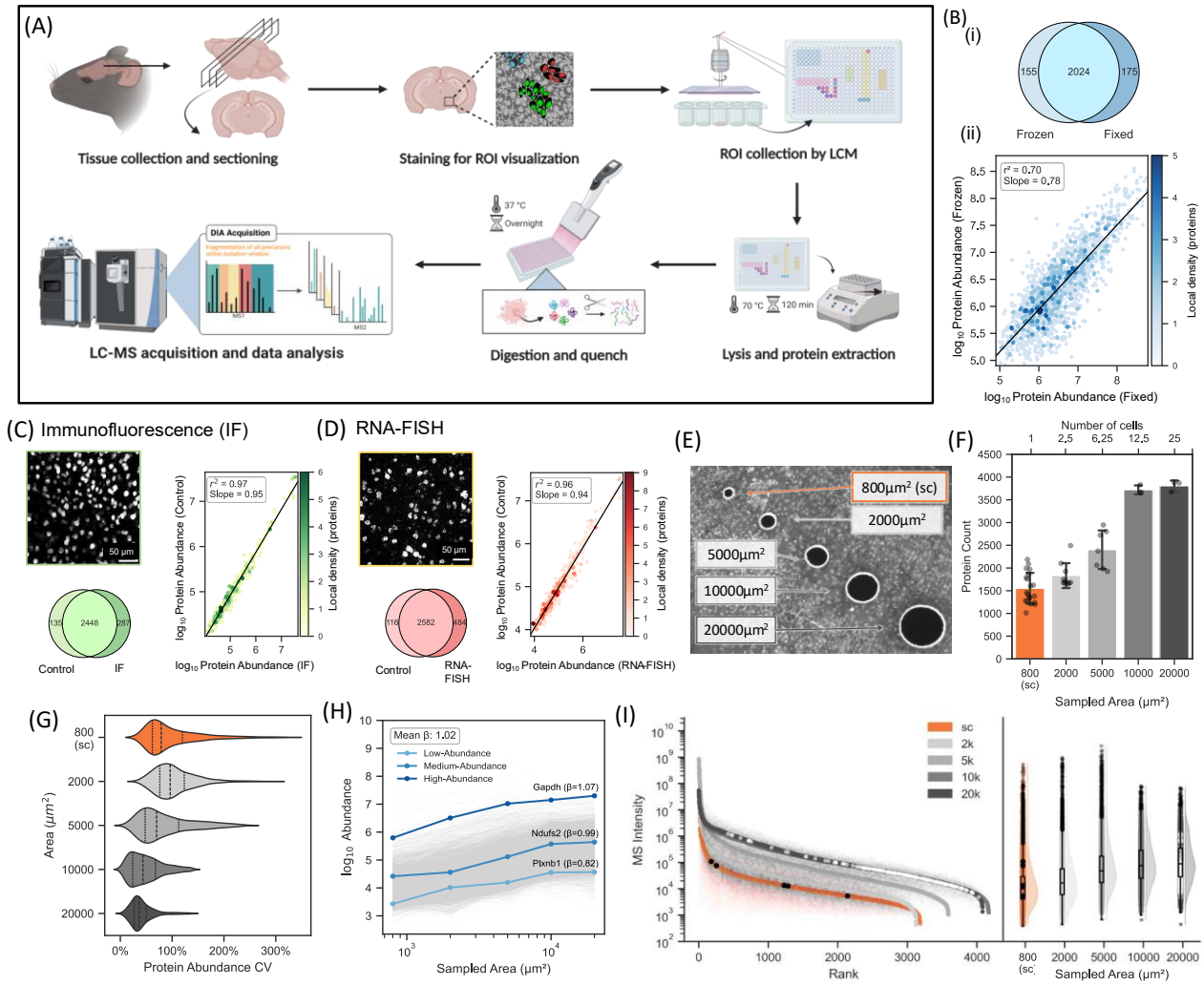

Figure 1: Validation and optimization of marker-guided spatial single-cell proteomics in CNS tissue: (A) Schematic overview of the LCM-based scSP workflow. Mouse brain tissue is fixed, cryosectioned, and stained with the desired marker panel, followed by LCM of regions of interest, lysis, digestion, and LC–MS analysis (Created in BioRender. Pang, W. (2025) https://BioRender.com/q97z901). **(B)** Comparison of proteomic profiles obtained from fresh-frozen and fixed bulk cortical tissue, showing protein identification overlap (top) and high correlation of log-transformed protein abundances between conditions (bottom). n = 3 animals **(C)** Effect of IF staining on scSP: representative NeuN-stained mouse cortical section. Scale bar: 50 µm (left, top), overlap of protein identifications between IF-stained samples and unstained (PBS) controls (left, bottom), and correlation of log protein abundances,

767 demonstrating minimal staining-induced bias (right). (n = 10 cells from IF-stained tissue, n = 9
768 from control tissue) **(D)** Effect of RNA-FISH mRNA staining on protein abundance, showing (i) a
769 representative cortical RNA-FISH image targeting GAD transcripts, (ii) protein identification
770 overlap, and (iii) abundance correlations relative to unstained controls, indicating negligible
771 impact of RNA-FISH on proteomic measurements. (n = 7 cells from FISH-stained tissue, n = 9
772 cells from control tissue). Scale bar: 50 μm **(E)** Representative NeuN-stained cortical regions
773 corresponding to approximately 1, 3, 6, 12, and 25 neuronal cell bodies (800, 2,000, 5,000,
774 10,000, and 20,000 μm^2; n = 20, 10, 7, 3, and 3, respectively). **(F)** Number of high-confidence
775 proteins ($q < 0.01$) identified across sampled areas. **(G)** Coefficients of variation (CVs) of protein
776 abundances across sampled areas, showing increased variability at the single-cell level,
777 consistent with greater biological heterogeneity compared to larger cortical regions. **(H)** Log–log
778 scaling of protein abundance as a function of sampled area, with a mean scaling exponent $\beta_1 \approx$
779 1.02, indicating near-linear scaling across proteins spanning low to high abundance (e.g.,
780 Plxnb1, Ndufs2, Gapdh). **(I)** Abundance–rank quantile and raincloud analyses showing proteins
781 uniquely detected in single-cell samples and those absent only from single-cell datasets, with
782 single-cell-specific proteins spanning a broad dynamic range, while proteins missing from
783 single-cell measurements were predominantly low-abundance species.

Figure 2

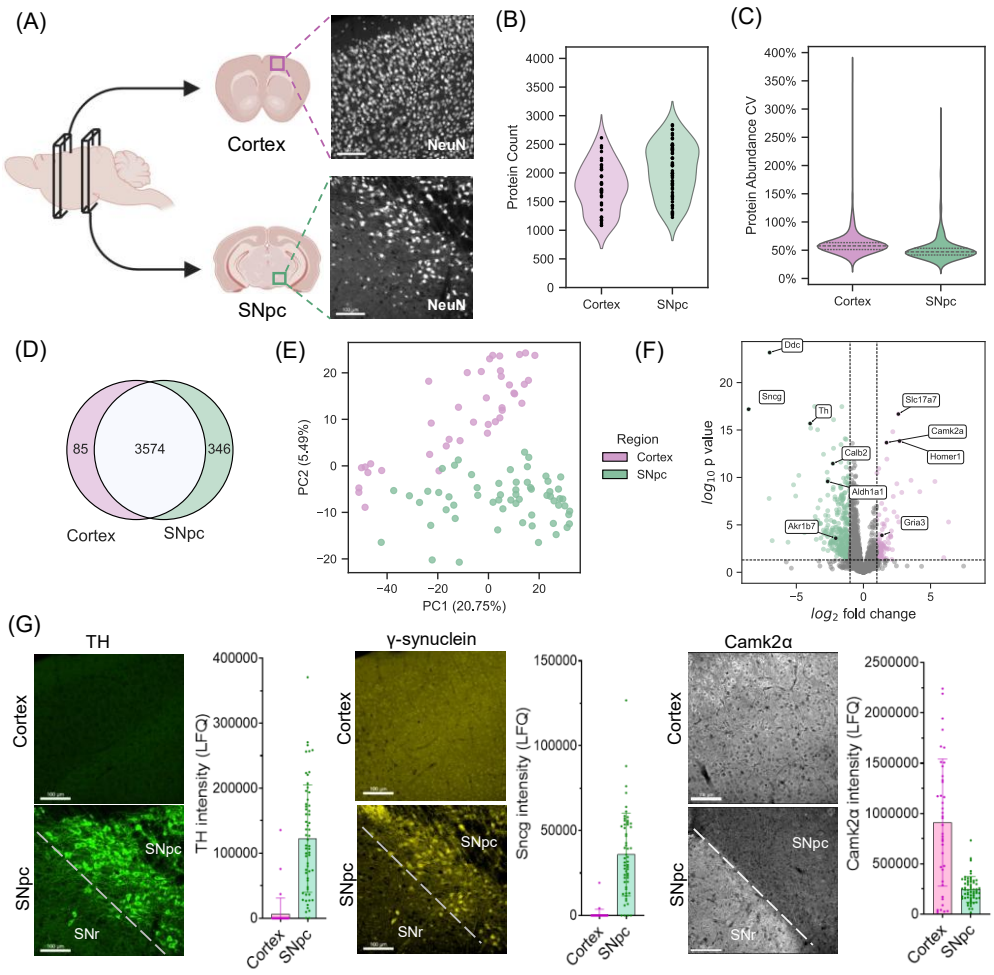

Figure 2: Characterization of CNS neuronal subpopulations using LCM-based scSP: (A) Schematic representation of the cortex and SNpc brain regions selected for comparison using LCM-based scSP. Representative confocal microscopy images showing immunostaining of neuronal cell bodies in the cortex and SNpc. Neurons are labeled with anti-NeuN. Created in BioRender. Dutta, S. (2026) https://BioRender.com/t68m928 (modified). Scale bar: 100 µm. **(B)** Protein counts from isolated single-cell samples obtained from cortical and SNpc regions using LCM-based scSP. (n= 60 cells for cortex; 40 cells for SNpc). **(C)** CVs of protein abundances for the groups showing comparable variance of around 50% for both groups. **(D)** Overlap of identified proteins between cortical and SNpc samples and proteins uniquely identified in each group. **(E)** Unsupervised PCA plot of protein intensities from the two sample groups showing cluster separation of single-cell samples from the cortex and SNpc. **(F)** Distribution of differentially expressed proteins (DEPs) between the cortex and SNpc. Proteins significantly

799 upregulated in each neuron type are highlighted, revealing region-specific protein markers. **(G)**
800 Corresponding IF validation using anti-TH, anti-gamma synuclein, and anti-Camk2α antibodies
801 to indicate protein expression distribution. The respective bar graphs illustrate the label-free
802 quantification (LFQ) mass spectrometry intensity levels of these marker proteins in each single-
803 cell sample.

Figure 3

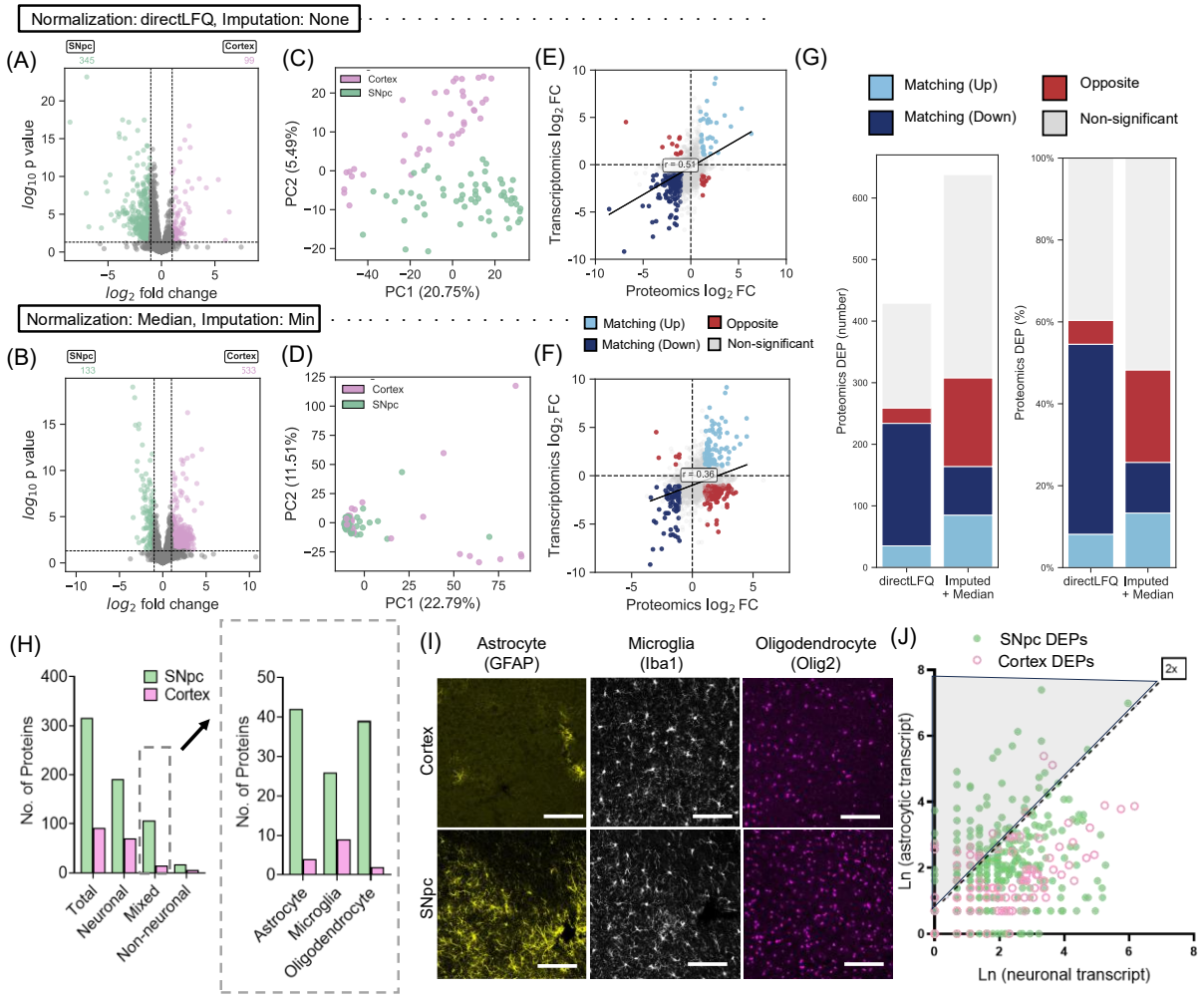

Figure 3: Single-cell transcriptomics informs data processing and refinement of neuronal proteomic assignments. (A–B) Distribution of DEPs between cortical and SNpc neurons using directLFQ quantification (A) or imputation (20% minimum value) followed by global median normalization (B), highlighting increased DEP detection and cortex-skewed upregulation with imputation. **(C–D)** Unsupervised PCA of single-neuron proteomes demonstrates improved separation of cortical and SNpc samples using directLFQ (C) compared to imputed data (D). **(E–F)** Cross-omics comparison of proteomic log_2 fold changes with single-cell transcriptomic cortex-to-SNpc ratios, color-coded by concordant upregulation, concordant downregulation, and opposite directionality, reveals higher concordance and correlation using directLFQ. **(G)** Quantification of agreement between proteomic and transcriptomic directionality shows higher overall concordance for directLFQ relative to imputed normalization. **(H)** Classification of DEPs based on Drop-seq transcriptomic enrichment using DropViz (i) classifies proteins as neuronal,

819 mixed, or non-neuronal. (ii) Stratification of mixed DEPs into confidence groups based on the
820 highest transcript levels among astrocytes, microglia, and oligodendrocytes, possible
821 contributors to background signal in SNpc proteomes. **(I)** IF staining of astrocytes, microglia,
822 and oligodendrocytes reveals greater astrocytic density in SNpc compared to cortex, confirming
823 astrocytes as major contributors to non-neuronal DEPs in SNpc samples. Scale bar 100 μm. (J)
824 Correlation plot of neuronal and astrocytic transcript abundance for DEPs visualizes cell-type-
825 specific expression patterns. Gray shaded area indicates DEPs of possible astrocytic origin.

Figure 4

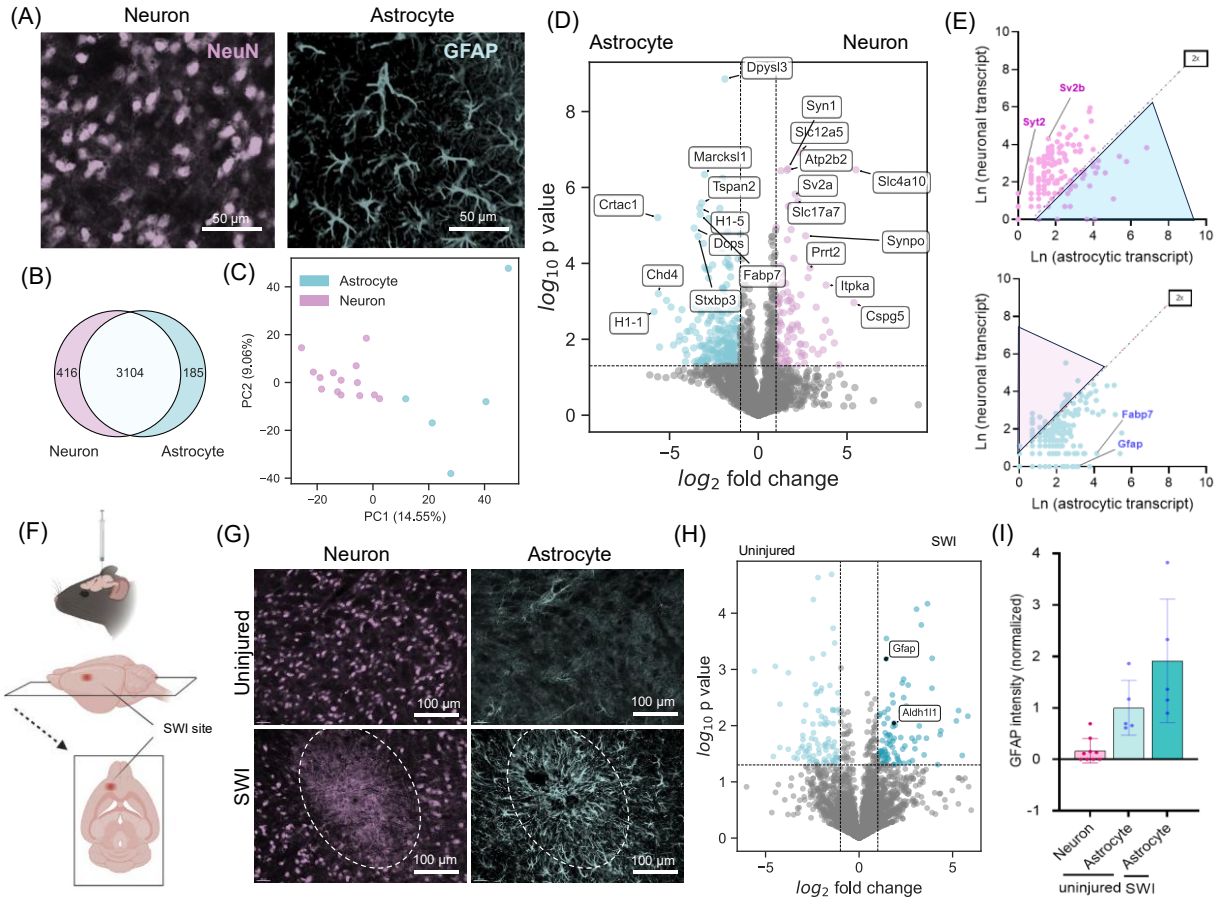

Figure 4. Single-cell spatial proteomics of astrocytes capture cell-type identity and neuroinflammatory activation. (A) Representative IF images of mouse brain sections stained for NeuN (neurons) and GFAP (astrocytes), enabling selective laser capture. Scale bars, 50 µm. **(B)** Venn diagram showing overlap and cell-type-specific protein groups identified across single neurons and astrocytes. (n= 14 cells for neuron; 5 cells for astrocyte) **(C)** Unsupervised PCA of single-cell proteomic profiles demonstrates clear separation between neuronal and astrocytic samples. **(D)** Volcano plot depicting differentially abundant proteins between astrocytes and neurons. Representative neuron-enriched and astrocyte-enriched proteins are annotated. **(E)** Integration of proteomic differential abundance with Drop-seq transcriptomic data, comparing astrocyte- and neuron-enriched proteins against corresponding astrocytic and neuronal transcript expression, respectively (shaded area highlights potential non-specific DEPs). **(F)** Schematic of the acute stab wound injury (SWI) model, illustrating the injury site. Created in BioRender. Dutta, S. (2026) https://BioRender.com/kye7fc7 (modified). **(G)** Representative IF

842 images of NeuN and GFAP in uninjured control tissue and at the SWI site. Scale bars, 100 μm.
843 **(H)** Differential abundance analysis of single astrocytes isolated from the peri-lesional SWI
844 region compared with astrocytes from contralateral uninjured tissue (n= 5 cells for uninjured; 5
845 cells for SWI). Proteins associated with astrocyte activation are highlighted. **(I)** Quantification of
846 mass spectrometry-derived GFAP intensities across neurons and astrocytes from uninjured and
847 SWI conditions, showing increased GFAP abundance in reactive astrocytes.

Figure 5

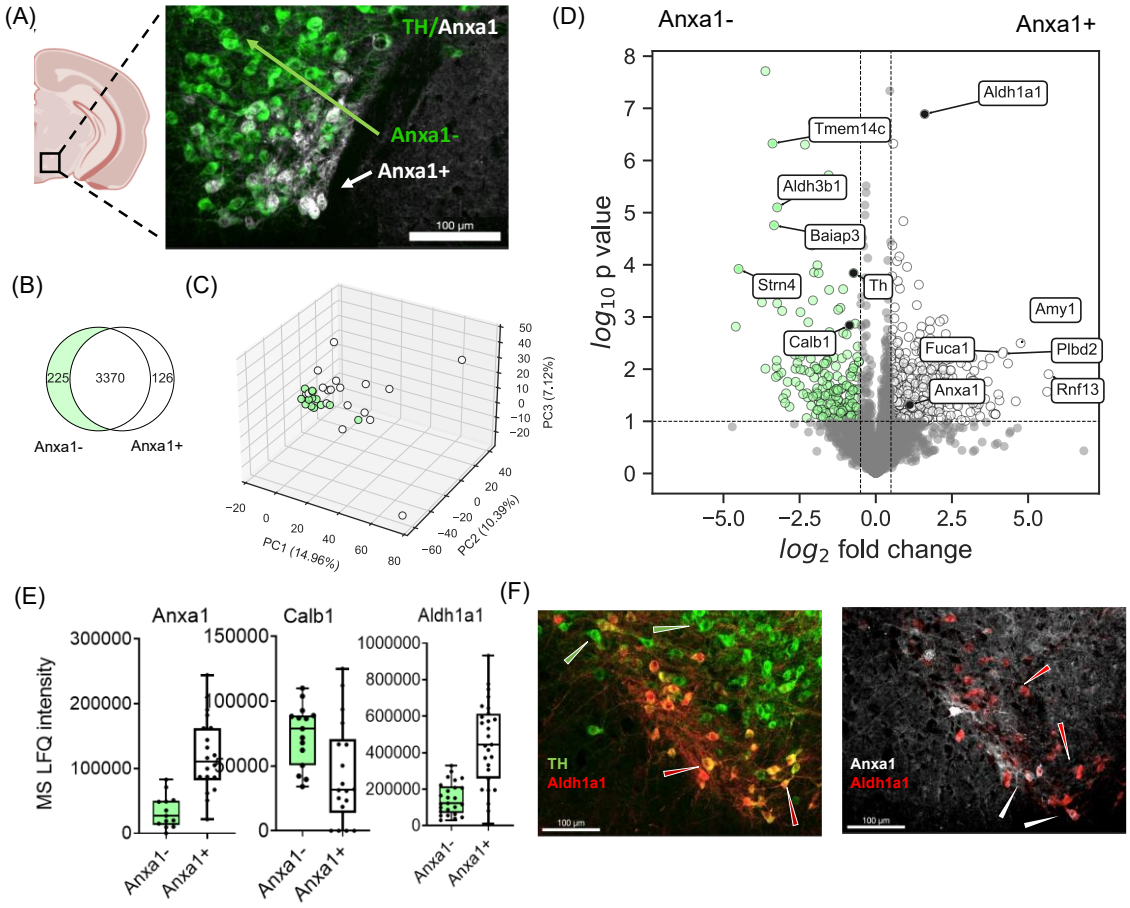

Figure 5: Proteomic differences between dorsal and ventral SNpc dopaminergic neuron subpopulations determined by scSP. (A) Schematic and representative IF image illustrating dual labeling of SNpc dopaminergic neurons with TH (green) and Anxa1 (white) to distinguish ventral-tier ($TH^+/Anxa1^+$) from dorsal-tier ($TH^+/Anxa1^-$) neurons. Scale bar, 100 µm. Created in BioRender. Dutta, S. (2026) https://BioRender.com/t5i05fp (modified). **(B)** Venn diagram showing overlap of identified protein groups across $TH^+/Anxa1^+$ and $TH^+/Anxa1^-$ single neurons, with population-specific proteins indicated (n = 18 cells for Anxa+; 15 cells for Anxa-). **(C)** PCA of profiles from $Anxa1^+$ and $Anxa1^-$ dopaminergic neurons **(D)** Differential protein abundance between $Anxa1^+$ and $Anxa1^-$ neurons, highlighting top proteins enriched in each sample group. **(E)** Protein abundance distributions for Anxa1, Calb1, and Aldh1a1 in $Anxa1^+$ and $Anxa1^-$ neurons, illustrating differential expression between the groups. **(F)** Representative IHC validation of higher expression of Aldh1a1 in the ventral SNpc neurons and lower or absent staining in the dorsal tier. Scale bar, 100 µm.

Figure 6

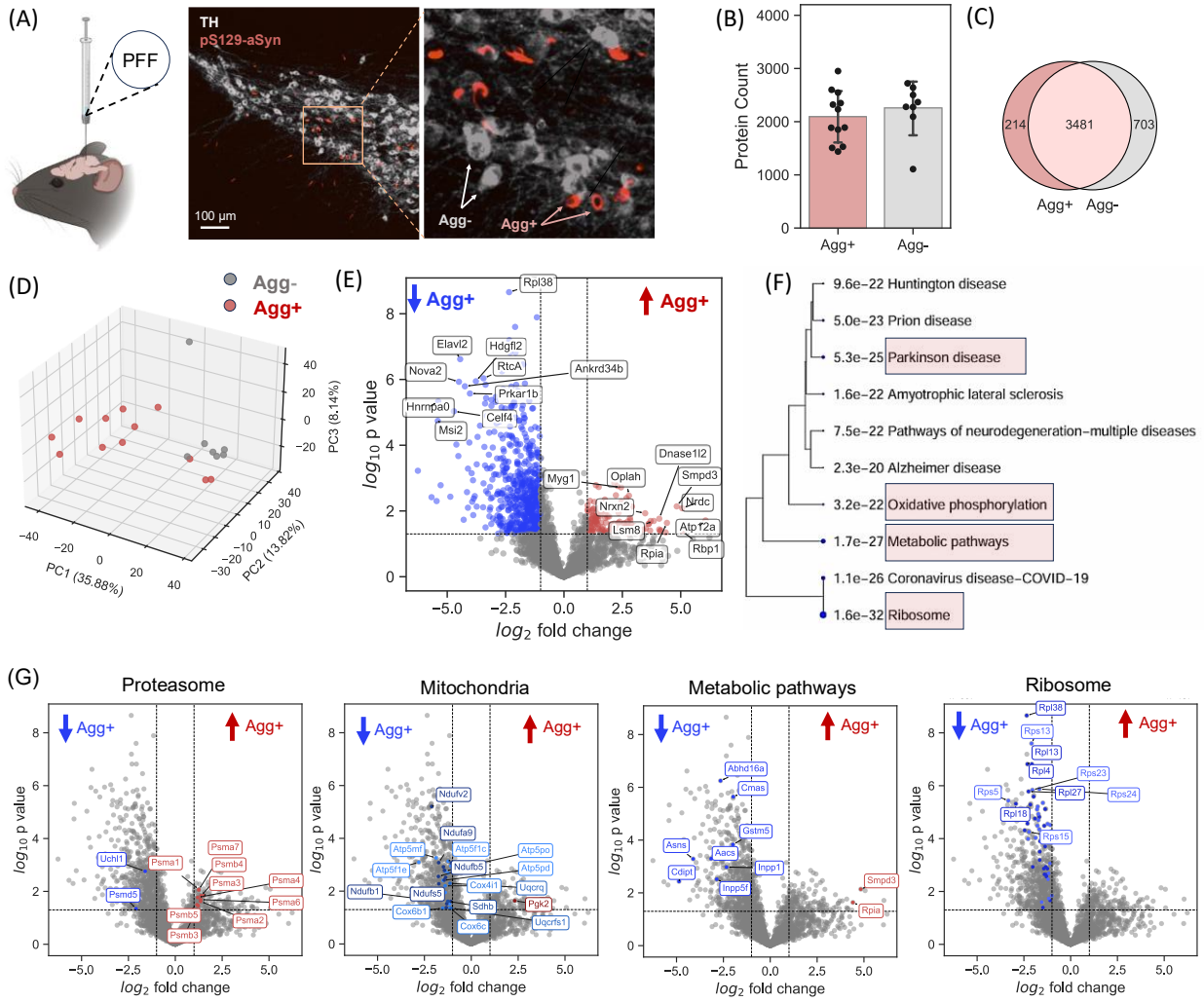

Figure 6. Proteomic profiling of α-synuclein aggregate–bearing SNpc neurons in a murine Parkinson's disease model. (A) Experimental overview and representative IF showing dopaminergic SNpc neurons labeled with TH and pathogenic phosphorylated α-synuclein (pS129-αSyn) aggregates, enabling identification and laser capture of aggregate-containing (Agg^+) and non-aggregate (Agg^-) neurons following intrastriatal injection of αSyn preformed fibrils (PFFs). Created in BioRender. Dutta, S. (2026) https://BioRender.com/s7wcjyf (modified). **(B)** Number of proteins identified per single neuron in Agg^+ and Agg^- populations (mean ± SD). (n= 12 cells for Agg+; 7 cells for Agg-) **(C)** Venn diagram showing overlapping and uniquely detected proteins between Agg^+ and Agg^- neurons. **(D)** Unsupervised PCA of single-cell proteomes, illustrating separation and increased variability of Agg^+ neurons. **(E)** Volcano plot of differential protein abundance between Agg^+ and Agg^- neurons (log_2 fold change versus $-log_{10}$

878 p value), with selected differentially abundant proteins annotated. **(F)** KEGG pathway
879 enrichment analysis of differentially abundant proteins showing top 10 implicated pathways. **(G)**
880 Pathway-focused volcano plots illustrating differential regulation of proteins associated with the
881 proteasome, mitochondrial oxidative phosphorylation, metabolic pathways, and the ribosome in
882 Agg^{+} neurons relative to Agg^{-} neurons.

Acknowledgments

This research was funded in part by Aligning Science Across Parkinson's (ASAP-020495 to V.G.) through the Michael J. Fox Foundation for Parkinson's Research (MJFF), the NIH R01MH136394 to M.L.R and T-F. C., Wellcome Leap Fellowship (through its Delta Tissue program) to M.L.R., and A*STAR National Science Scholarship (BS-PhD) to M.P. V.G. is an Investigator of the Howard Hughes Medical Institute. For the purpose of open access, the authors have applied a CC BY public copyright license to all Author Accepted Manuscripts arising from this submission.

We thank the CNSI Advanced Light Microscopy/Spectroscopy Facility at UCLA and Leica Biosystems for access to the LCM instruments.

Conflict of Interest

The authors declare no competing financial interests.

Author contributions:

S.D. conceived the overall study. S.D. and M.P. designed the experiments, performed LCM sample collection, data analysis, and visualization, and prepared the manuscript with input from all authors. S.D. conducted stereotaxic surgery, tissue processing, immunohistology staining, Drop-seq analysis, and imaging. M.P conducted proteomics sample preparation, mass spectrometry data acquisition, and all proteomics data processing and analysis, as well as single-cell transcriptomics data analysis. G.M.C. designed and processed samples for RNA-FISH experiments. S.G. assisted with tissue processing, staining, and data visualization plots. M.L.R. advised on single-cell proteomics experiments and instrumentation. T-F.C. supervised proteomics experiments and data analysis. V.G. supervised the overall study and advised on experimental design.

Data Availability

The data, code, protocols, and key lab materials used and generated in this study are listed in a Key Resource Table alongside their persistent identifiers (**Supp. Table 1**). The proteomics datasets are available on MassIVE MSV000100704 or ProteomeXchange PXD074008.

Code Availability

All analysis scripts used in this study at available at https://github.com/gnaprs/scSP_CNS-preprint.

913 **References**

914 1. Herculano-Houzel, S. (2009). The human brain in numbers: a linearly scaled-up primate
915 brain. Front Hum Neurosci *3*, 31. 10.3389/neuro.09.031.2009.
916 2. Hondius, D.C., Koopmans, F., Leistner, C., Pita-Illobre, D., Peferoen-Baert, R.M.,
917 Marbus, F., Paliukhovich, I., Li, K.W., Rozemuller, A.J.M., Hoozemans, J.J.M., and Smit,
918 A.B. (2021). The proteome of granulovacuolar degeneration and neurofibrillary tangles in
919 Alzheimer's disease. Acta Neuropathol *141*, 341-358. 10.1007/s00401-020-02261-4.
920 3. Harding, A.J., and Halliday, G.M. (2001). Cortical Lewy body pathology in the diagnosis
921 of dementia. Acta Neuropathol *102*, 355-363. 10.1007/s004010100390.
922 4. Kamath, T., Abdulraouf, A., Burris, S.J., Langlieb, J., Gazestani, V., Nadaf, N.M.,
923 Balderrama, K., Vanderburg, C., and Macosko, E.Z. (2022). Single-cell genomic profiling
924 of human dopamine neurons identifies a population that selectively degenerates in
925 Parkinson's disease. Nat Neurosci *25*, 588-595. 10.1038/s41593-022-01061-1.
926 5. Piwecka, M., Rajewsky, N., and Rybak-Wolf, A. (2023). Single-cell and spatial
927 transcriptomics: deciphering brain complexity in health and disease. Nat Rev Neurol *19*,
928 346-362. 10.1038/s41582-023-00809-y.
929 6. Zhong, J., Tang, G., Zhu, J., Wu, W., Li, G., Lin, X., Liang, L., Chai, C., Zeng, Y., Wang,
930 F., et al. (2021). Single-cell brain atlas of Parkinson's disease mouse model. J Genet
931 Genomics *48*, 277-288. 10.1016/j.jgg.2021.01.003.
932 7. Yang, L., Ball, A., Liu, J., Jain, T., Li, Y.M., Akhter, F., Zhu, D., and Wang, J. (2022).
933 Cyclic microchip assay for measurement of hundreds of functional proteins in single
934 neurons. Nat Commun *13*, 3548. 10.1038/s41467-022-31336-x.
935 8. Zhang, D., Rubio Rodriguez-Kirby, L.A., Lin, Y., Wang, W., Song, M., Wang, L., Wang, L.,
936 Kanatani, S., Jimenez-Beristain, T., Dang, Y., et al. (2025). Spatial dynamics of brain
937 development and neuroinflammation. Nature *647*, 213-227. 10.1038/s41586-025-09663-
938 y.
939 9. Chen, C., McDonald, D., Blain, A., Sachdeva, A., Bone, L., Smith, A.L.M., Warren, C.,
940 Pickett, S.J., Hudson, G., Filby, A., et al. (2021). Imaging mass cytometry reveals
941 generalised deficiency in OXPHOS complexes in Parkinson's disease. NPJ Parkinsons
942 Dis *7*, 39. 10.1038/s41531-021-00182-x.
943 10. Jung, S.Y., Choi, J.M., Rousseaux, M.W., Malovannaya, A., Kim, J.J., Kutzera, J., Wang,
944 Y., Huang, Y., Zhu, W., Maity, S., et al. (2017). An Anatomically Resolved Mouse Brain
945 Proteome Reveals Parkinson Disease-relevant Pathways. Mol Cell Proteomics *16*, 581-
946 593. 10.1074/mcp.M116.061440.

947 11. Zhu, Y., Dou, M., Piehowski, P.D., Liang, Y., Wang, F., Chu, R.K., Chrisler, W.B., Smith,
948 J.N., Schwarz, K.C., Shen, Y., et al. (2018). Spatially Resolved Proteome Mapping of
949 Laser Capture Microdissected Tissue with Automated Sample Transfer to Nanodroplets.
950 Mol Cell Proteomics *17*, 1864-1874. 10.1074/mcp.TIR118.000686.
951 12. Griesser, E., Wyatt, H., Ten Have, S., Stierstorfer, B., Lenter, M., and Lamond, A.I.
952 (2020). Quantitative Profiling of the Human Substantia Nigra Proteome from Laser-
953 capture Microdissected FFPE Tissue. Mol Cell Proteomics *19*, 839-851.
954 10.1074/mcp.RA119.001889.
955 13. Budnik, B., Levy, E., Harmange, G., and Slavov, N. (2018). SCoPE-MS: mass
956 spectrometry of single mammalian cells quantifies proteome heterogeneity during cell
957 differentiation. Genome Biol *19*, 161. 10.1186/s13059-018-1547-5.
958 14. Zhu, Y., Piehowski, P.D., Zhao, R., Chen, J., Shen, Y., Moore, R.J., Shukla, A.K., Petyuk,
959 V.A., Campbell-Thompson, M., Mathews, C.E., et al. (2018). Nanodroplet processing
960 platform for deep and quantitative proteome profiling of 10-100 mammalian cells. Nat
961 Commun *9*, 882. 10.1038/s41467-018-03367-w.
962 15. Schoof, E.M., Furtwangler, B., Uresin, N., Rapin, N., Savickas, S., Gentil, C., Lechman,
963 E., Keller, U.A.D., Dick, J.E., and Porse, B.T. (2021). Quantitative single-cell proteomics
964 as a tool to characterize cellular hierarchies. Nat Commun *12*, 3341. 10.1038/s41467-
965 021-23667-y.
966 16. Brunner, A.D., Thielert, M., Vasilopoulou, C., Ammar, C., Coscia, F., Mund, A., Hoerning,
967 O.B., Bache, N., Apalategui, A., Lubeck, M., et al. (2022). Ultra-high sensitivity mass
968 spectrometry quantifies single-cell proteome changes upon perturbation. Mol Syst Biol
969 *18*, e10798. 10.15252/msb.202110798.
970 17. Gebreyesus, S.T., Siyal, A.A., Kitata, R.B., Chen, E.S., Enkhbayar, B., Angata, T., Lin,
971 K.I., Chen, Y.J., and Tu, H.L. (2022). Streamlined single-cell proteomics by an integrated
972 microfluidic chip and data-independent acquisition mass spectrometry. Nat Commun *13*,
973 37. 10.1038/s41467-021-27778-4.
974 18. Ctortecka, C., Hartlmayr, D., Seth, A., Mendjan, S., Tourniaire, G., Udeshi, N.D., Carr,
975 S.A., and Mechtler, K. (2023). An Automated Nanowell-Array Workflow for Quantitative
976 Multiplexed Single-Cell Proteomics Sample Preparation at High Sensitivity. Mol Cell
977 Proteomics *22*, 100665. 10.1016/j.mcpro.2023.100665.
978 19. Rosenberger, F.A., Thielert, M., Strauss, M.T., Schweizer, L., Ammar, C., Madler, S.C.,
979 Metousis, A., Skowronek, P., Wahle, M., Madden, K., et al. (2023). Spatial single-cell

980 mass spectrometry defines zonation of the hepatocyte proteome. Nat Methods *20*, 1530-
981 1536. 10.1038/s41592-023-02007-6.
982 20. Xiang, P., Liyu, A., Kwon, Y., Hu, D., Williams, S.M., Velickovic, D., Markillie, L.M.,
983 Chrisler, W.B., Pasa-Tolic, L., and Zhu, Y. (2023). Spatial Proteomics toward Subcellular
984 Resolution by Coupling Deep Ultraviolet Laser Ablation with Nanodroplet Sample
985 Preparation. ACS Meas Sci Au *3*, 459-468. 10.1021/acsmeasuresciau.3c00033.
986 21. Mund, A., Coscia, F., Kriston, A., Hollandi, R., Kovacs, F., Brunner, A.D., Migh, E.,
987 Schweizer, L., Santos, A., Bzorek, M., et al. (2022). Deep Visual Proteomics defines
988 single-cell identity and heterogeneity. Nat Biotechnol *40*, 1231-1240. 10.1038/s41587-
989 022-01302-5.
990 22. Pang, M., Jones, J.J., Wang, T.Y., Quan, B., Kubat, N.J., Qiu, Y., Roukes, M.L., and
991 Chou, T.F. (2024). Increasing Proteome Coverage Through a Reduction in Analyte
992 Complexity in Single-Cell Equivalent Samples. J Proteome Res.
993 10.1021/acs.jproteome.4c00062.
994 23. Matzinger, M., Muller, E., Durnberger, G., Pichler, P., and Mechtler, K. (2023). Robust
995 and Easy-to-Use One-Pot Workflow for Label-Free Single-Cell Proteomics. Anal Chem
996 *95*, 4435-4445. 10.1021/acs.analchem.2c05022.
997 24. Lein, E.S., Hawrylycz, M.J., Ao, N., Ayres, M., Bensinger, A., Bernard, A., Boe, A.F.,
998 Boguski, M.S., Brockway, K.S., Byrnes, E.J., et al. (2007). Genome-wide atlas of gene
999 expression in the adult mouse brain. Nature *445*, 168-176. 10.1038/nature05453.
1000 25. Lazar, C., Gatto, L., Ferro, M., Bruley, C., and Burger, T. (2016). Accounting for the
1001 Multiple Natures of Missing Values in Label-Free Quantitative Proteomics Data Sets to
1002 Compare Imputation Strategies. J Proteome Res *15*, 1116-1125.
1003 10.1021/acs.jproteome.5b00981.
1004 26. Vanderaa, C., and Gatto, L. (2023). Revisiting the Thorny Issue of Missing Values in
1005 Single-Cell Proteomics. J Proteome Res *22*, 2775-2784.
1006 10.1021/acs.jproteome.3c00227.
1007 27. Stelloo, S., Alejo-Vinogradova, M.T., van Gelder, C., Zijlmans, D.W., van Oostrom, M.J.,
1008 Valverde, J.M., Lamers, L.A., Rus, T., Sobrevals Alcaraz, P., Schafers, T., et al. (2024).
1009 Deciphering lineage specification during early embryogenesis in mouse gastruloids
1010 using multilayered proteomics. Cell Stem Cell *31*, 1072-1090 e1078.
1011 10.1016/j.stem.2024.04.017.
1012 28. Bubis, J.A., Arrey, T.N., Damoc, E., Delanghe, B., Slovakova, J., Sommer, T.M., Kagawa,
1013 H., Pichler, P., Rivron, N., Mechtler, K., and Matzinger, M. (2025). Challenging the Astral

1014 mass analyzer to quantify up to 5,300 proteins per single cell at unseen accuracy to
1015 uncover cellular heterogeneity. Nat Methods *22*, 510-519. 10.1038/s41592-024-02559-1.
1016 29. Webel, H., Niu, L., Nielsen, A.B., Locard-Paulet, M., Mann, M., Jensen, L.J., and
1017 Rasmussen, S. (2024). Imputation of label-free quantitative mass spectrometry-based
1018 proteomics data using self-supervised deep learning. Nat Commun *15*, 5405.
1019 10.1038/s41467-024-48711-5.
1020 30. Ammar, C., Schessner, J.P., Willems, S., Michaelis, A.C., and Mann, M. (2023). Accurate
1021 Label-Free Quantification by directLFQ to Compare Unlimited Numbers of Proteomes.
1022 Mol Cell Proteomics *22*, 100581. 10.1016/j.mcpro.2023.100581.
1023 31. Yao, Z., van Velthoven, C.T.J., Kunst, M., Zhang, M., McMillen, D., Lee, C., Jung, W.,
1024 Goldy, J., Abdelhak, A., Aitken, M., et al. (2023). A high-resolution transcriptomic and
1025 spatial atlas of cell types in the whole mouse brain. Nature *624*, 317-332.
1026 10.1038/s41586-023-06812-z.
1027 32. Taniguchi, Y., Choi, P.J., Li, G.W., Chen, H., Babu, M., Hearn, J., Emili, A., and Xie, X.S.
1028 (2010). Quantifying E. coli proteome and transcriptome with single-molecule sensitivity in
1029 single cells. Science *329*, 533-538. 10.1126/science.1188308.
1030 33. Fulcher, J.M., Markillie, L.M., Mitchell, H.D., Williams, S.M., Engbrecht, K.M., Degnan,
1031 D.J., Bramer, L.M., Moore, R.J., Chrisler, W.B., Cantlon-Bruce, J., et al. (2024). Parallel
1032 measurement of transcriptomes and proteomes from same single cells using
1033 nanodroplet splitting. Nat Commun *15*, 10614. 10.1038/s41467-024-54099-z.
1034 34. Darmanis, S., Gallant, C.J., Marinescu, V.D., Niklasson, M., Segerman, A., Flamourakis,
1035 G., Fredriksson, S., Assarsson, E., Lundberg, M., Nelander, S., et al. (2016).
1036 Simultaneous Multiplexed Measurement of RNA and Proteins in Single Cells. Cell Rep
1037 *14*, 380-389. 10.1016/j.celrep.2015.12.021.
1038 35. Saunders, A., Macosko, E.Z., Wysoker, A., Goldman, M., Krienen, F.M., de Rivera, H.,
1039 Bien, E., Baum, M., Bortolin, L., Wang, S., et al. (2018). Molecular Diversity and
1040 Specializations among the Cells of the Adult Mouse Brain. Cell *174*, 1015-1030 e1016.
1041 10.1016/j.cell.2018.07.028.
1042 36. Allen, N.J., and Barres, B.A. (2009). Neuroscience: Glia - more than just brain glue.
1043 Nature *457*, 675-677. 10.1038/457675a.
1044 37. Zuchero, J.B., and Barres, B.A. (2015). Glia in mammalian development and disease.
1045 Development *142*, 3805-3809. 10.1242/dev.129304.
1046 38. Koupourtidou, C., Schwarz, V., Aliee, H., Frerich, S., Fischer-Sternjak, J., Bocchi, R.,
1047 Simon-Ebert, T., Bai, X., Sirko, S., Kirchhoff, F., et al. (2024). Shared inflammatory glial

1048 cell signature after stab wound injury, revealed by spatial, temporal, and cell-type-
1049 specific profiling of the murine cerebral cortex. Nat Commun *15*, 2866. 10.1038/s41467-
1050 024-46625-w.
1051 39. Gaertner, Z., Azcorra, M., Dombeck, D.A., and Awatramani, R. (2022). Molecular
1052 heterogeneity in the substantia nigra: A roadmap for understanding PD motor
1053 pathophysiology. Neurobiol Dis *175*, 105925. 10.1016/j.nbd.2022.105925.
1054 40. Azcorra, M., Gaertner, Z., Davidson, C., He, Q., Kim, H., Nagappan, S., Hayes, C.K.,
1055 Ramakrishnan, C., Fenno, L., Kim, Y.S., et al. (2023). Unique functional responses
1056 differentially map onto genetic subtypes of dopamine neurons. Nat Neurosci *26*, 1762-
1057 1774. 10.1038/s41593-023-01401-9.
1058 41. Poulin, J.F., Zou, J., Drouin-Ouellet, J., Kim, K.Y., Cicchetti, F., and Awatramani, R.B.
1059 (2014). Defining midbrain dopaminergic neuron diversity by single-cell gene expression
1060 profiling. Cell Rep *9*, 930-943. 10.1016/j.celrep.2014.10.008.
1061 42. Poulin, J.F., Gaertner, Z., Moreno-Ramos, O.A., and Awatramani, R. (2020).
1062 Classification of Midbrain Dopamine Neurons Using Single-Cell Gene Expression
1063 Profiling Approaches. Trends Neurosci *43*, 155-169. 10.1016/j.tins.2020.01.004.
1064 43. Henderson, M.X., Cornblath, E.J., Darwich, A., Zhang, B., Brown, H., Gathagan, R.J.,
1065 Sandler, R.M., Bassett, D.S., Trojanowski, J.Q., and Lee, V.M.Y. (2019). Spread of
1066 alpha-synuclein pathology through the brain connectome is modulated by selective
1067 vulnerability and predicted by network analysis. Nat Neurosci *22*, 1248-1257.
1068 10.1038/s41593-019-0457-5.
1069 44. Goralski, T.M., Meyerdirk, L., Breton, L., Brasseur, L., Kurgat, K., DeWeerd, D., Turner,
1070 L., Becker, K., Adams, M., Newhouse, D.J., and Henderson, M.X. (2024). Spatial
1071 transcriptomics reveals molecular dysfunction associated with cortical Lewy pathology.
1072 Nat Commun *15*, 2642. 10.1038/s41467-024-47027-8.
1073 45. Volpicelli-Daley, L.A., Kirik, D., Stoyka, L.E., Standaert, D.G., and Harms, A.S. (2016).
1074 How can rAAV-alpha-synuclein and the fibril alpha-synuclein models advance our
1075 understanding of Parkinson's disease? J Neurochem *139 Suppl 1*, 131-155.
1076 10.1111/jnc.13627.
1077 46. Volpicelli-Daley, L.A., Luk, K.C., Patel, T.P., Tanik, S.A., Riddle, D.M., Stieber, A.,
1078 Meaney, D.F., Trojanowski, J.Q., and Lee, V.M. (2011). Exogenous alpha-synuclein fibrils
1079 induce Lewy body pathology leading to synaptic dysfunction and neuron death. Neuron
1080 *72*, 57-71. 10.1016/j.neuron.2011.08.033.

1081 47. Chung, H.K., Ho, H.A., Perez-Acuna, D., and Lee, S.J. (2019). Modeling alpha-
1082 Synuclein Propagation with Preformed Fibril Injections. J Mov Disord *12*, 139-151.
1083 10.14802/jmd.19046.
1084 48. Kanehisa, M., Furumichi, M., Sato, Y., Matsuura, Y., and Ishiguro-Watanabe, M. (2025).
1085 KEGG: biological systems database as a model of the real world. Nucleic Acids Res *53*,
1086 D672-D677. 10.1093/nar/gkae909.
1087 49. Nordmann, T.M., Anderton, H., Hasegawa, A., Schweizer, L., Zhang, P., Stadler, P.C.,
1088 Sinha, A., Metousis, A., Rosenberger, F.A., Zwiebel, M., et al. (2024). Spatial proteomics
1089 identifies JAKi as treatment for a lethal skin disease. Nature *635*, 1001-1009.
1090 10.1038/s41586-024-08061-0.
1091 50. Method of the Year 2024: spatial proteomics. (2024). Nat Methods *21*, 2195-2196.
1092 10.1038/s41592-024-02565-3.
1093 51. Rosenberger, F.A., Madler, S.C., Thorhauge, K.H., Steigerwald, S., Fromme, M.,
1094 Lebedev, M., Weiss, C.A.M., Oeller, M., Wahle, M., Metousis, A., et al. (2025). Deep
1095 Visual Proteomics maps proteotoxicity in a genetic liver disease. Nature *642*, 484-491.
1096 10.1038/s41586-025-08885-4.
1097 52. Ding, S.L., Royall, J.J., Sunkin, S.M., Ng, L., Facer, B.A., Lesnar, P., Guillozet-
1098 Bongaarts, A., McMurray, B., Szafer, A., Dolbeare, T.A., et al. (2016). Comprehensive
1099 cellular-resolution atlas of the adult human brain. J Comp Neurol *524*, 3127-3481.
1100 10.1002/cne.24080.
1101 53. Jiang, Y.R., Zhu, L., Cao, L.R., Wu, Q., Chen, J.B., Wang, Y., Wu, J., Zhang, T.Y., Wang,
1102 Z.L., Guan, Z.Y., et al. (2023). Simultaneous deep transcriptome and proteome profiling
1103 in a single mouse oocyte. Cell Rep *42*, 113455. 10.1016/j.celrep.2023.113455.
1104 54. de Sousa Abreu, R., Penalva, L.O., Marcotte, E.M., and Vogel, C. (2009). Global
1105 signatures of protein and mRNA expression levels. Mol Biosyst *5*, 1512-1526.
1106 10.1039/b908315d.
1107 55. Doorn, J.A., Florang, V.R., Schamp, J.H., and Vanle, B.C. (2014). Aldehyde
1108 dehydrogenase inhibition generates a reactive dopamine metabolite autotoxic to
1109 dopamine neurons. Parkinsonism Relat Disord *20 Suppl 1*, S73-75. 10.1016/S1353-
1110 8020(13)70019-1.
1111 56. Poewe, W., Seppi, K., Tanner, C.M., Halliday, G.M., Brundin, P., Volkmann, J., Schrag,
1112 A.E., and Lang, A.E. (2017). Parkinson disease. Nat Rev Dis Primers *3*, 17013.
1113 10.1038/nrdp.2017.13.

1114 57. Moon, H.E., and Paek, S.H. (2015). Mitochondrial Dysfunction in Parkinson's Disease.
1115 Exp Neurobiol *24*, 103-116. 10.5607/en.2015.24.2.103.
1116 58. Wang, X., Becker, K., Levine, N., Zhang, M., Lieberman, A.P., Moore, D.J., and Ma, J.
1117 (2019). Pathogenic alpha-synuclein aggregates preferentially bind to mitochondria and
1118 affect cellular respiration. Acta Neuropathol Commun *7*, 41. 10.1186/s40478-019-0696-4.
1119 59. Bishop, P., Rocca, D., and Henley, J.M. (2016). Ubiquitin C-terminal hydrolase L1 (UCH-
1120 L1): structure, distribution and roles in brain function and dysfunction. Biochem J *473*,
1121 2453-2462. 10.1042/BCJ20160082.
1122 60. Dutta, S., Pang, M., Donahue, R.R., Chou, T., Seifert, A.W., and Gradinaru, V. (2025).
1123 Parkinson's disease modeling in regenerative spiny mice (Acomys dimidiatus) captures
1124 key disease-relevant behavioral, histological, and molecular signatures. bioRxiv.
1125 https://doi.org/10.1101/2025.11.06.687049.
1126 61. Garcia-Esparcia, P., Hernandez-Ortega, K., Koneti, A., Gil, L., Delgado-Morales, R.,
1127 Castano, E., Carmona, M., and Ferrer, I. (2015). Altered machinery of protein synthesis
1128 is region- and stage-dependent and is associated with alpha-synuclein oligomers in
1129 Parkinson's disease. Acta Neuropathol Commun *3*, 76. 10.1186/s40478-015-0257-4.
1130 62. Jang, Y., Pletnikova, O., Troncoso, J.C., Pantelyat, A.Y., Dawson, T.M., Rosenthal, L.S.,
1131 and Na, C.H. (2023). Mass Spectrometry-Based Proteomics Analysis of Human
1132 Substantia Nigra From Parkinson's Disease Patients Identifies Multiple Pathways
1133 Potentially Involved in the Disease. Mol Cell Proteomics *22*, 100452.
1134 10.1016/j.mcpro.2022.100452.
1135 63. Ma, S.X., Seo, B.A., Kim, D., Xiong, Y., Kwon, S.H., Brahmachari, S., Kim, S., Kam, T.I.,
1136 Nirujogi, R.S., Kwon, S.H., et al. (2021). Complement and Coagulation Cascades are
1137 Potentially Involved in Dopaminergic Neurodegeneration in alpha-Synuclein-Based
1138 Mouse Models of Parkinson's Disease. J Proteome Res *20*, 3428-3443.
1139 10.1021/acs.jproteome.0c01002.
1140 64. Ping, L., Duong, D.M., Yin, L., Gearing, M., Lah, J.J., Levey, A.I., and Seyfried, N.T.
1141 (2018). Global quantitative analysis of the human brain proteome in Alzheimer's and
1142 Parkinson's Disease. Sci Data *5*, 180036. 10.1038/sdata.2018.36.
1143 65. Werner, C.J., Heyny-von Haussen, R., Mall, G., and Wolf, S. (2008). Proteome analysis
1144 of human substantia nigra in Parkinson's disease. Proteome Sci *6*, 8. 10.1186/1477-
1145 5956-6-8.
1146 66. Killinger, B.A., Marshall, L.L., Chatterjee, D., Chu, Y., Bras, J., Guerreiro, R., and
1147 Kordower, J.H. (2022). In situ proximity labeling identifies Lewy pathology molecular

1148 interactions in the human brain. Proc Natl Acad Sci U S A *119*.
1149 10.1073/pnas.2114405119.
1150 67. Gatto, L., Aebersold, R., Cox, J., Demichev, V., Derks, J., Emmott, E., Franks, A.M.,
1151 Ivanov, A.R., Kelly, R.T., Khoury, L., et al. (2023). Initial recommendations for performing,
1152 benchmarking and reporting single-cell proteomics experiments. Nat Methods *20*, 375-
1153 386. 10.1038/s41592-023-01785-3.
1154 68. Bhatia, H.S., Brunner, A.D., Ozturk, F., Kapoor, S., Rong, Z., Mai, H., Thielert, M., Ali, M.,
1155 Al-Maskari, R., Paetzold, J.C., et al. (2022). Spatial proteomics in three-dimensional
1156 intact specimens. Cell *185*, 5040-5058 e5019. 10.1016/j.cell.2022.11.021.
1157 69. Choi, H.M.T., Schwarzkopf, M., Fornace, M.E., Acharya, A., Artavanis, G., Stegmaier, J.,
1158 Cunha, A., and Pierce, N.A. (2018). Third-generation in situ hybridization chain reaction:
1159 multiplexed, quantitative, sensitive, versatile, robust. Development *145*.
1160 10.1242/dev.165753.
1161 70. Jang, M.J., Coughlin, G.M., Jackson, C.R., Chen, X., Chuapoco, M.R., Vendemiatti, J.L.,
1162 Wang, A.Z., and Gradinaru, V. (2023). Spatial transcriptomics for profiling the tropism of
1163 viral vectors in tissues. Nat Biotechnol *41*, 1272-1286. 10.1038/s41587-022-01648-w.
1164 71. Eng, J.K., McCormack, A.L., and Yates, J.R. (1994). An approach to correlate tandem
1165 mass spectral data of peptides with amino acid sequences in a protein database. J Am
1166 Soc Mass Spectrom *5*, 976-989. 10.1016/1044-0305(94)80016-2.
1167 72. Zolg, D.P., Gessulat, S., Paschke, C., Graber, M., Rathke-Kuhnert, M., Seefried, F.,
1168 Fitzemeier, K., Berg, F., Lopez-Ferrer, D., Horn, D., et al. (2021). INFERYS rescoring:
1169 Boosting peptide identifications and scoring confidence of database search results.
1170 Rapid Commun Mass Spectrom, e9128. 10.1002/rcm.9128.
1171 73. Kall, L., Canterbury, J.D., Weston, J., Noble, W.S., and MacCoss, M.J. (2007). Semi-
1172 supervised learning for peptide identification from shotgun proteomics datasets. Nat
1173 Methods *4*, 923-925. 10.1038/nmeth1113.
1174 74. Brenes, A.J. (2024). Calculating and Reporting Coefficients of Variation for DIA-Based
1175 Proteomics. J Proteome Res *23*, 5274-5278. 10.1021/acs.jproteome.4c00461.
1176 75. Wolf, F.A., Angerer, P., and Theis, F.J. (2018). SCANPY: large-scale single-cell gene
1177 expression data analysis. Genome Biol *19*, 15. 10.1186/s13059-017-1382-0.
1178 76. Pang, M. (2025). scpviz: v0.5.2-alpha. Zenodo.
1179 77. Szklarczyk, D., Nastou, K., Koutrouli, M., Kirsch, R., Mehryary, F., Hachilif, R., Hu, D.,
1180 Peluso, M.E., Huang, Q., Fang, T., et al. (2025). The STRING database in 2025: protein

1181 networks with directionality of regulation. Nucleic Acids Res *53*, D730-D737.
1182 10.1093/nar/gkae1113.